

NASA CONTRACTOR REPORT 166385

NASA-CR-166385
19820024498

Math Modeling for Helicopter Simulation of Low Speed, Low Altitude and
Steeply Descending Flight

Philip F. Sheridan
Carl Robinson
Dr. John Shaw
Fred White

LIBRARY COPY

SEP 1 1982

LANGLEY RESEARCH CENTER
LIBRARY NASA
HAMPTON, VIRGINIA

CONTRACT NAS2-10975
July 1982

NASA



NF02642

Math Modeling for Helicopter Simulation of Low Speed, Low Altitude and
Steeply Descending Flight

Philip F. Sheridan
Carl Robinson
Dr. John Shaw
Fred White
Boeing Vertol Company
Philadelphia, Pennsylvania

Prepared for
Ames Research Center
under Contract NAS2-10975



National Aeronautics and
Space Administration

Ames Research Center
Moffett Field, California 94035

1182-32371/1

FOREWORD

This report was prepared for the NASA Ames Research Center under Contract Number NAS2-10975 by the Boeing Vertol Company and documents the research effort performed under that contract during the period June 1981 to June 1982

It deals with the development of a set of modifications to a helicopter math model for a better representation of low speed, low altitude, and steeply descending flight. Funding for the program was provided by NASA and was performed by members of the Flying Qualities staff of Boeing Vertol. Mr. Philip Sheridan and Dr. John Shaw were the Project Engineers. The test pilot for the simulation was Mr. A. L. Freisner of Flight Test, and the programmer for the simulation was Mr. K. J. Ezzell of the Boeing Computer Services Company. Technical monitoring was provided by Mr. William A. Decker of the Flight Dynamics and Control Branch, NASA Ames, and the Contract Administrator was Harry M. King, NASA Ames. The Boeing Vertol Contract Representative was Mr. J. M. Oakes.

The Flying Qualities staff at Boeing Vertol would like to acknowledge further Mr. Philip F. Sheridan, who died suddenly in August 1981. Mr. Sheridan made many contributions to the understanding of helicopter interactional aerodynamics and flying qualities concepts in general, and his expertise will be missed.

TABLE OF CONTENTS

	<u>PAGE</u>
LIST OF FIGURES	iv
LIST OF TABLES	vi
LIST OF SYMBOLS	vii
SUMMARY	1
INTRODUCTION	2
MODEL FORMULATION	
LOW SPEED AND GROUND PROXIMITY EFFECTS	3
STEEP DESCENT EFFECTS	18
MODEL CHECK OUT	
MODEL IMPLEMENTATION ON BOEING VERTOL SIMULATOR	31
SIMULATION RESULTS	41
CONCLUSIONS	49
REFERENCES	50
APPENDIX	51

LIST OF FIGURES

<u>FIGURE</u>		<u>PAGE</u>
1	Tip Path Plane Dynamics	4
2	Main Rotor Forces and Moments	5
3	Equations for the Solution of Flapping and Inflow Coefficients	11
4	Low Speed, Low Altitude Inflow Derivation Scheme	13
5	Low Speed, Low Altitude Wind Tunnel Test Conditions	14
6	Effect of Ground Proximity on Steady Induced Inflow Coefficient	15
7	Effect of Ground Proximity on Longitudinal Inflow Coefficient	16
8	Effect of Ground Proximity on Lateral Inflow Coefficient	17
9	Effect of Angle of Attack on the Steady Induced Inflow Coefficient	19
10	Effect of Angle of Attack on the Longitudinal Inflow Coefficient	20
11	Effect of Angle of Attack on the Lateral Inflow Coefficient	21
12	Effect of Disc Loading on the Steady Induced Inflow Coefficient	22
13	Effect of Disc Loading on the Longitudinal Inflow Coefficient	23
14	Effect of Disc Loading on the Lateral Inflow Coefficient	24
15	Induced Velocity Plots From Reference 4	26
16	Expanded Thrust Fluctuation Curves From Reference 4	27
17	Periodicity of Thrust Fluctuations	28
18	Modifications to Simulation Model	32
19	Effect of Ground Proximity on Lateral Trim	42
20	Effect of Modifications on Lateral Trim	43

LIST OF FIGURES (CONT'D)

<u>FIGURE</u>		<u>PAGE</u>
21	Effect of Rate of Descent on Thrust Fluctuations	46
22	Effect of a Collective Pull Up at a High Rate of Descent	47
23	Increased Power Required Due to Vortex - Ring State	48

LIST OF TABLES

<u>TABLE</u>		<u>PAGE</u>
1	Steady Induced Inflow Ratio in Descending Flight ($\lambda'_{oI}/\sqrt{C_T/2}$)	34
2	Change in Steady Induced Inflow Ratio Due to Ground Proximity ($\Delta\lambda'_{oI}/\sqrt{C_T/2}$)	35
3	Effect of Ground Proximity on Longitudinal First Harmonic Inflow Ratio ($\lambda'_1/\sqrt{C_T/2}$)	36
4	Change in Steady Induced Inflow Ratio Due to Angle of Attack ($\Delta\lambda''_{oI}/\sqrt{C_T/2}$)	37
5	Change in Longitudinal First Harmonic Inflow Ratio Due to Angle of Attack ($\Delta\lambda''_1/\sqrt{C_T/2}$)	38
6	Magnitude of Thrust Fluctuations in Descending Flight ($\Delta T/T$)	40
A-1	Main Rotor Blade Physical Properties	51
A-2	Wind Tunnel Data Used in the Determination of Low Speed, Low Altitude Inflow Coefficients	52

LIST OF SYMBOLS

- A_{1c} lateral cyclic pitch measured from hub plane and in "wind-hub" system, rad
- a blade lift-curve slope
- a_1 longitudinal first-harmonic flapping coefficient measured from hub plane and in "wind-hub" system, rad
- \dot{a}_1 rate of change of a_1 with time, rad/sec
- a_0 blade coning angle measured from hub plane, rad
- \dot{a}_0 rate of change of a_0 with time, rad/sec
- B_{1c} longitudinal cyclic pitch measured from hub plane and in "wind-hub" system, rad
- b_1 lateral first-harmonic flapping coefficient measured from hub plane and in "wind-hub" system, rad
- \dot{b}_1 rate of change of b_1 with time, rad/sec
- C_H H force coefficient, $C_H = \frac{H_F}{\rho\pi R^2(\Omega R)^2}$
- C_Q torque coefficient, $C_Q = \frac{Q_F}{\rho\pi R^2(\Omega R)^2 R}$
- C_T thrust coefficient, $C_T = \frac{T_F}{\rho\pi R^2(\Omega R)^2}$
- C_Y Y force coefficient, $C_Y = \frac{Y_F}{\rho\pi R^2(\Omega R)^2}$
- c blade chord, m
- d main rotor diameter, m
- DL Disc Loading, N/M^2 (or PSF)
- e flapping hinge offset, m
- h main rotor hub height above the ground, m

- H_F component of main rotor resultant force in the rotor disc plane in $\psi' = 0$ direction, N
- I_β blade moment of inertia about flapping hinge, kg-m^2
- K_1 pitch-flap coupling ratio, $\tan \delta_3$
- K_β flapping hinge restraint, N-m/rad
- L_H rolling hub moment in hub-body system
- L_{HF} main rotor hub moment about x'_s axis, N-m
- M_H pitching hub moment in hub-body system
- M_{HF} main rotor hub moment about y'_s axis, N-m
- M_β blade mass moment about the flapping hinge, kg-m
- N number of blades
- P ratio of flapping frequency to rotor system angular velocity
- p aircraft roll rate, rad/sec
- p_w aircraft roll rate in wind-hub system rad/sec, $p_w = p \cos \beta_w + q \sin \beta_w$
- \ddot{p} aircraft roll acceleration, rad/sec^2
- Q_F main rotor torque about z'_s axis, N-m
- q aircraft pitch rate, rad/sec
- q_w aircraft pitch rate in wind-hub system, rad/sec, $q_w = -p \sin \beta_w + q \cos \beta_w$
- \dot{q} aircraft pitch acceleration, rad/sec^2

R rotor radius, m

r aircraft yaw rate, rad/sec

r' radial station of the blade element measured from the flapping hinge, m

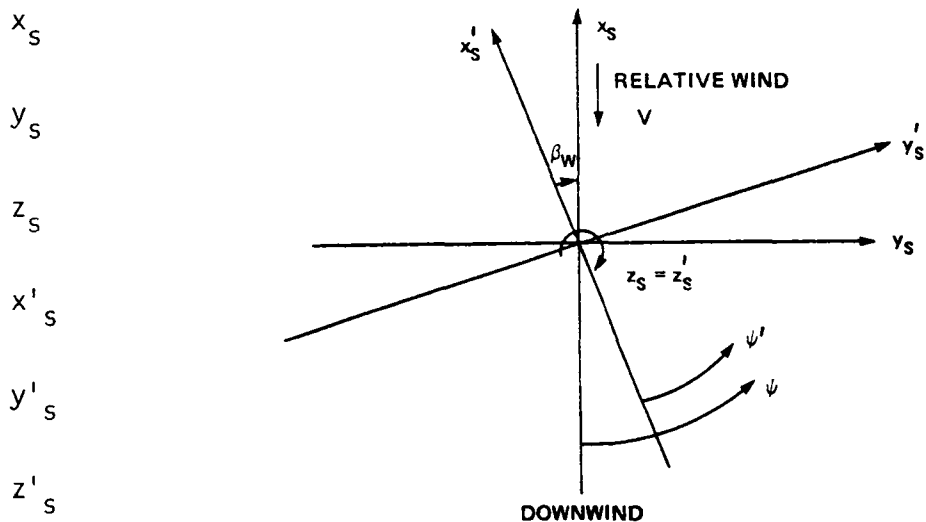
T_F main rotor thrust force acting perpendicular to rotor disc plane, N

ΔT magnitude of thrust fluctuation, N

V true airspeed, m/sec

v_i uniform induced velocity, $v_i = \frac{C_T(\Omega R)}{2\sqrt{\mu^2 + \lambda_0^2}}$, m/sec

x nondimensional radial station of the blade element, $x \triangleq \frac{e + r'}{R}$

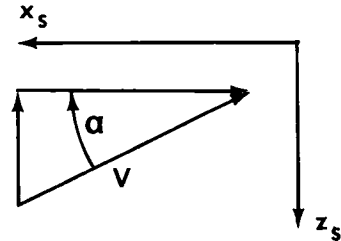


x'_s, y'_s, z'_s = ROTOR "HUB-BODY" SYSTEM

x_s, y_s, z_s = ROTOR "HUB-WIND" SYSTEM

Y_F component of main rotor resultant force in the rotor disc plane in $\psi' = 90^\circ$ direction, N

α hub disc plane angle of attack, deg (or rad)



β blade flapping angle measured from hub plane, rad

β_w rotor sideslip angle, that is, the angle between x_s and x'_s , rad

γ Lock number, $\frac{\rho a c R^4}{I_\beta}$

δ blade mean profile drag coefficient

ε e/R

θ blade pitch angle measured from hub plane,

$$\theta = \theta_0 - A_{1c} \cos \psi - B_{1c} \sin \psi + x\theta_t - K_1\beta, \text{ rad}$$

θ_0 blade-root collective pitch measured from hub plane, rad

θ_t total blade twist (tip with respect to root), rad

ω_v frequency of thrust fluctuation, rad/sec

μ advance ratio, $\frac{V \cos \alpha}{\Omega R}$

ρ air density, kg/m^3

σ rotor solidity ratio

ψ azimuth angle measured from downwind in the sense of rotor rotation, rad

ψ' azimuth angle measured from $-x'_s$ in the sense of rotor rotation, rad

Ω rotor system angular velocity, rad/sec

λ local inflow,

$$\lambda = \lambda_0 + x (\lambda_1 \cos \psi + \lambda_2 \sin \psi)$$

λ_{oI} uniform induced inflow ratio, $v_i/\Omega R$

λ_0 inflow ratio at rotor disc center,

$$\lambda_0 = \frac{V \sin \alpha - v_i}{\Omega R}$$

λ_{oh} inflow ratio at hover, $\sqrt{C_T}/2$

λ_1 First harmonic longitudinal inflow coefficient

λ_2 First harmonic lateral inflow coefficient

λ'_{oI} Uniform induced inflow ratio in the simulation model from either momentum theory equation or vortex-ring table

$\Delta\lambda'_{oI}$ Increment in uniform induced inflow ratio in the simulation model due to ground proximity

$\Delta\lambda''_{oI}$ Increment in uniform induced inflow ratio in the simulation model due to angle of attack variation

λ_1' Longitudinal inflow coefficient in the simulation model from the ground proximity table

$\Delta\lambda_1''$ Increment in longitudinal inflow coefficient in the simulation model due to angle of attack variation

λ_{0I}'' Total uniform induced inflow ratio in the simulation model prior to dynamic lag

λ_1'' Total longitudinal inflow coefficient in the simulation model prior to dynamic lag

SUMMARY

A math model has been formulated to represent some of the aerodynamic effects of low speed, low altitude, and steeply descending flight. The formulation is intended to be consistent with the single rotor real time simulation model at NASA Ames Research Center.

The effect of low speed, low altitude flight on main rotor downwash was obtained by assuming a uniform plus first harmonic inflow model and then by using wind tunnel data in the form of hub loads, solve for the inflow coefficients. The result was a set of tables for steady and first harmonic inflow coefficients as functions of ground proximity, angle of attack, and airspeed.

The aerodynamics associated with steep descending flight in the vortex-ring state were modeled by replacing the steady induced downwash derived from momentum theory with an experimentally derived value and by including a thrust fluctuations effect due to vortex shedding. Tables of the induced downwash and the magnitude of the thrust fluctuations were created as functions of angle of attack and airspeed.

INTRODUCTION

Ground based simulators provide a safe means for conducting research to develop control systems and to insure safe flight procedures. However, for these simulations to be effective, an acceptable representation of the desired flight characteristics must be modeled. Several flight regimes important to helicopter handling qualities pose special modeling problems. Two of these regimes are low-speed transition from hovering to forward flight, in and out of ground effect, and rates of descent in the vortex-ring state.

Part of the modeling problem in these regimes rests with the main rotor inflow representation. The current helicopter handling qualities simulation model at NASA Ames Research Center uses uniform downwash derived from momentum theory in calculating rotor aerodynamic forces and moments. The present study modifies the Ames model by providing a more accurate representation of the main rotor inflow field for these two flight regimes.

In the case of the low-speed transition problem, the first step was to include two first harmonic terms in the inflow model. The equations for main rotor flapping and main rotor forces and moments were then rederived to include these additional terms. Finally, wind tunnel data, in the form of rotor forces and moments, was combined with the rederived rotor equations to solve for the inflow coefficients. Various flight conditions were investigated and tables of inflow values were generated.

For the vortex-ring problem, published experimental data of steady induced downwash was curve fitted and put in tabular form. In addition to the inflow representation, thrust fluctuations were included to approximate some of the unsteady nature of this flight regime.

In each case, the tabular parameters were nondimensionalized.

MODEL FORMULATION

LOW SPEED, AND GROUND PROXIMITY EFFECTS

The first step in modifying the simulation model was to recognize the need for a more sophisticated inflow model. The present handling qualities simulation model at NASA Ames assumes uniform downwash. A number of people, such as References 3 and 6, have shown that by including a longitudinal harmonic inflow term, predictive values for lateral flapping during low-speed flight correlated better with test values. The form of the inflow model assumed in this study was

$$\lambda = \lambda_0 + \chi \lambda_1 \cos \psi + \chi \lambda_2 \sin \psi$$

Using this inflow model, the equations for main rotor flapping and main rotor forces and moments from Reference 1 were rederived. Figure 1 presents the three flapping equations with the coefficients of the additional harmonic inflow terms appearing in the last two columns of the last matrix. This result was also developed in Reference 6. Figure 2 shows the equations for main rotor forces and moments with the additional terms underlined.

The next step was to choose a set of equations to use with wind tunnel data to solve for the inflow coefficients. Using the measured main rotor hub loads and the input parameters, this set of equations would then be solved simultaneously for λ_0 , λ_1 , and λ_2 . Since the flapping coefficients a_0 , a_1 , and b_1 were also assumed unknown, this required a set of at least six equations.

The first set of equations chosen consisted of the two first harmonic flapping equations of Figure 1, along with the equations for rotor thrust, hub moments, and rotor torque from Figure 2. This set of equations yielded solutions which were considered to be inconsistent. The test used for consistency was simply to insert the solutions for λ_0 , λ_1 , and λ_2 back into the flapping equations and compare the two answers for a_0 , a_1 and b_1 . It was found that the values for coning did not match. Since the coning equation was not included in the λ_0 , λ_1 , and λ_2 solution this is not totally unexpected. Because of this inconsistency it was decided to look for another combination of equations.

$$\ddot{\underline{a}} + \ddot{\underline{D}}\underline{a} + \ddot{\underline{K}}\underline{a} = \ddot{\underline{f}}$$

$$\ddot{\underline{D}} = \Omega^2 \begin{bmatrix} \frac{\gamma}{2} \left(\frac{1}{4} - \frac{2}{3} \epsilon + \frac{\epsilon^2}{2} \right) & 0 & -\frac{\gamma\mu}{4} \left(\frac{1}{3} - \epsilon + \epsilon^2 \right) \\ 0 & \frac{\gamma}{2} \left(\frac{1}{4} - \frac{2}{3} \epsilon + \frac{\epsilon^2}{2} \right) & 2 \\ -\frac{\gamma\mu}{2} \left(\frac{1}{3} - \epsilon + \epsilon^2 \right) & -2 & \frac{\gamma}{2} \left(\frac{1}{4} - \frac{2}{3} \epsilon + \frac{\epsilon^2}{2} \right) \end{bmatrix}$$

$$\ddot{\underline{K}} = \Omega^2 \begin{bmatrix} p^2 + \frac{\gamma K_1 \mu^2}{4} \left(\frac{1}{2} - \epsilon + \frac{\epsilon^2}{2} \right) & -\frac{\gamma\mu}{4} \left(\frac{\epsilon}{2} - \epsilon^2 \right) & -\frac{\gamma K_1 \mu}{4} \left(\frac{2}{3} - \epsilon \right) \\ -\frac{\gamma\mu}{2} \left(\frac{1}{3} - \frac{\epsilon}{2} \right) & p^2 - 1 + \frac{\gamma K_1 \mu^2}{8} \left(\frac{1}{2} - \epsilon + \frac{\epsilon^2}{2} \right) & \frac{\gamma}{2} \left(\frac{1}{4} - \frac{2}{3} \epsilon + \frac{\epsilon^2}{2} \right) + \frac{\gamma\mu^2}{8} \times \left(\frac{1}{2} - \epsilon + \frac{\epsilon^2}{2} \right) \\ -\frac{\gamma K_1 \mu}{2} \left(\frac{2}{3} - \epsilon \right) & -\frac{\gamma}{2} \left(\frac{1}{4} - \frac{2}{3} \epsilon + \frac{\epsilon^2}{2} \right) + \frac{\gamma\mu^2}{8} \times \left(\frac{1}{2} - \epsilon + \frac{\epsilon^2}{2} \right) & p^2 - 1 + \frac{3}{8} \gamma K_1 \mu^2 \left(\frac{1}{2} - \epsilon + \frac{\epsilon^2}{2} \right) \end{bmatrix}$$

$$\ddot{\underline{f}} = \Omega^2 \begin{bmatrix} \frac{\gamma}{2} \left[\left(\frac{1}{4} - \frac{\epsilon}{3} \right) + \frac{\mu^2}{2} \times \left(\frac{1}{2} - \epsilon + \frac{\epsilon^2}{2} \right) \right] & \frac{\gamma}{2} \left[\left(\frac{1}{3} - \frac{\epsilon}{4} \right) + \frac{\mu^2}{2} \times \left(\frac{1}{3} - \frac{\epsilon}{2} \right) \right] & 0 & -\frac{\gamma\mu}{2} \left(\frac{1}{3} - \frac{\epsilon}{2} \right) \\ 0 & 0 & \frac{\gamma}{2} \left[\left(\frac{1}{4} - \frac{\epsilon}{3} \right) + \frac{\mu^2}{4} \times \left(\frac{1}{2} - \epsilon + \frac{\epsilon^2}{2} \right) \right] & 0 \\ -\frac{\gamma}{2} \mu \left(\frac{2}{3} - \epsilon \right) & -\frac{\gamma\mu}{2} \left(\frac{1}{2} - \frac{2\epsilon}{3} \right) & 0 & \frac{\gamma}{2} \left[\left(\frac{1}{4} - \frac{\epsilon}{3} \right) + \frac{3\mu^2}{4} \times \left(\frac{1}{2} - \epsilon + \frac{\epsilon^2}{2} \right) \right] \end{bmatrix} \begin{bmatrix} \theta_0 \\ \theta_t \\ A_{1c} \\ B_{1c} \end{bmatrix}$$

$$+ \Omega^2 \begin{bmatrix} \frac{\gamma\mu}{8\Omega} \left(\frac{2}{3} - \epsilon \right) & 0 \\ -\frac{2}{\Omega} \left(1 + \frac{eM_B}{I_B} \right) & -\frac{\gamma}{2\Omega} \left(\frac{1}{4} - \frac{\epsilon}{3} \right) \\ -\frac{\gamma}{2\Omega} \left(\frac{1}{4} - \frac{\epsilon}{3} \right) & \frac{2}{\Omega} \left(1 + \frac{eM_B}{I_B} \right) \end{bmatrix} \begin{bmatrix} p_v \\ q_v \end{bmatrix} - \begin{bmatrix} \frac{M_B g}{I_B} \\ 0 \\ 0 \end{bmatrix}$$

$$+ \Omega^2 \begin{bmatrix} \frac{\gamma}{2} \left(\frac{1}{3} - \frac{\epsilon}{2} \right) & 0 & \frac{\gamma\mu}{8} \left(\frac{2}{3} - \epsilon \right) \\ 0 & -\frac{\gamma}{2} \left(\frac{1}{4} - \frac{\epsilon}{3} \right) & 0 \\ -\frac{\gamma\mu}{2} \left(\frac{1}{2} - \epsilon + \frac{\epsilon^2}{2} \right) & 0 & -\frac{\gamma}{2} \left(\frac{1}{4} - \frac{\epsilon}{3} \right) \end{bmatrix} \begin{bmatrix} \lambda_0 \\ \lambda_1 \\ \lambda_2 \end{bmatrix}$$

$$\underline{a} = (a_0, a_1, b_1)^T ; \quad \beta(t) = a_0(t) - a_1(t) \cos \psi - b_1(t) \sin \psi$$

$$p^2 = 1 + \frac{K_B}{I_B \Omega^2} + \frac{eM_B}{I_B} + \frac{\gamma K_1}{8} \left(1 - \frac{4}{3} \epsilon \right)$$

FIGURE 1. TIP PATH PLANE DYNAMICS

Main Rotor Thrust

The main rotor thrust expression for a nonteetering rotor is:

$$\begin{aligned}
 T_F = \frac{N}{2} \rho a c R (\Omega R)^2 & \left\{ \frac{1}{2} (1 - \epsilon^2) \lambda_0 + \theta_0 \left[\frac{1}{3} + \frac{\mu^2}{2} (1 - \epsilon) \right] + \theta_t \left[\frac{1}{4} + \frac{\mu^2}{4} (1 - \epsilon^2) \right] \right. \\
 & - \frac{\mu}{2} (1 - \epsilon^2) (B_{1c} - K_1 b_1) - a_0 \left[\frac{1}{3} + \frac{\mu^2}{2} (1 - \epsilon) \right] K_1 + a_1 \left[\frac{\mu}{2} \epsilon (1 - \epsilon) \right] \\
 & - \frac{\dot{a}_0}{\Omega} \left(\frac{1}{3} - \frac{\epsilon}{2} \right) + \frac{\dot{b}_1}{\Omega} \left[\frac{\mu}{4} (1 - \epsilon)^2 \right] + \frac{\mu}{4} (1 - \epsilon^2) \lambda_2 \\
 & \left. + \frac{\mu}{4} (1 - \epsilon^2) \left(\frac{p}{\Omega} \cos \beta_w + \frac{q}{\Omega} \sin \beta_w \right) \right\} - N M_{\beta} \ddot{a}_0
 \end{aligned}$$

Main Rotor H and Y Forces in Hub-Body System

The expressions for the main rotor H and Y forces in the hub-body system are:

$$\begin{aligned}
 H_F &= \frac{N}{2} \rho a c R (\Omega R)^2 \frac{2C_H}{a\sigma} \\
 Y_F &= \frac{N}{2} \rho a c R (\Omega R)^2 \frac{2C_Y}{a\sigma}
 \end{aligned}$$

where

$$\begin{aligned}
 \frac{2C_H}{a\sigma} &= \left(\frac{2C_H}{a\sigma} \right)_w \cos \beta_w + \left(\frac{2C_Y}{a\sigma} \right)_w \sin \beta_w \\
 \frac{2C_Y}{a\sigma} &= - \left(\frac{2C_H}{a\sigma} \right)_w \sin \beta_w + \left(\frac{2C_Y}{a\sigma} \right)_w \cos \beta_w
 \end{aligned}$$

where $(2C_H/a\sigma)_w$ and $(2C_Y/a\sigma)_w$ are in the wind-hub system and are given by

FIGURE 2. MAIN ROTOR FORCES AND MOMENTS

$$\begin{aligned}
\left(\frac{2C_H}{a\sigma}\right)_w &= \frac{\delta\mu}{2a} (1 - \epsilon^2) - \frac{1}{4} (\theta_0 - K_1 a_0) \left[2\lambda_0 \mu (1 - \epsilon) - \mu (1 - \epsilon)^2 \frac{\dot{a}_0}{\Omega} \right. \\
&\quad \left. - \left(\epsilon - \frac{2}{3} \right) \left(\frac{\dot{b}_1}{\Omega} - a_1 \right) - \frac{2}{3} a_1 + \frac{2}{3} \left(\frac{p}{\Omega} \cos \beta_w + \frac{q}{\Omega} \sin \beta_w \right) \right] \\
&\quad - \frac{\theta_t}{4} \left[\mu \lambda_0 (1 - \epsilon^2) + \frac{\dot{a}_0}{\Omega} \mu \left(\epsilon - \frac{2}{3} \right) - 2 \left(\frac{\epsilon}{3} - \frac{1}{4} \right) \left(\frac{\dot{b}_1}{\Omega} - a_1 \right) - \frac{a_1}{2} \right. \\
&\quad \left. + \frac{1}{2} \left(\frac{p}{\Omega} \cos \beta_w + \frac{q}{\Omega} \sin \beta_w \right) \right] + \frac{1}{4} (A_{1c} - K_1 a_1) \left[-\frac{b_1 \mu}{4} (1 - \epsilon^2) \right. \\
&\quad \left. + \frac{1}{4} \mu (1 - \epsilon)^2 \left(\frac{\dot{a}_1}{\Omega} + b_1 \right) + \frac{2}{3} a_0 + \frac{\mu}{4} (1 - \epsilon^2) \left(-\frac{p}{\Omega} \sin \beta_w + \frac{q}{\Omega} \cos \beta_w \right) \right] \\
&\quad + \frac{1}{4} (B_{1c} - K_1 b_1) \left[\frac{3}{4} \mu (1 - \epsilon)^2 \left(\frac{\dot{b}_1}{\Omega} - a_1 \right) + (1 - \epsilon^2) \left(\lambda_0 - \frac{a_1 \mu}{4} \right) + \left(\epsilon - \frac{2}{3} \right) \frac{\dot{a}_0}{\Omega} \right. \\
&\quad \left. + \frac{3\mu}{4} (1 - \epsilon^2) \left(\frac{p}{\Omega} \cos \beta_w + \frac{q}{\Omega} \sin \beta_w \right) \right] + \frac{1}{4} \left\{ \epsilon (1 - \epsilon) \left(\frac{\dot{b}_1}{\Omega} - a_1 \right) 4\lambda_0 \right. \\
&\quad \left. - (1 - \epsilon^2) \left[2\lambda_0 \left(\frac{\dot{b}_1}{\Omega} - a_1 \right) - a_1 \lambda_0 \right] - \left(\frac{2}{3} - \epsilon \right) \left[a_1 \frac{\dot{a}_0}{\Omega} + a_0 \left(\frac{\dot{a}_1}{\Omega} + b_1 \right) \right] \right. \\
&\quad \left. - \frac{2a_0}{3} \left(-\frac{p}{\Omega} \sin \beta_w + \frac{q}{\Omega} \cos \beta_w \right) - \left[2(1 - \epsilon^2) \lambda_0 - 4 \left(\frac{1}{3} - \frac{\epsilon}{2} \right) \frac{\dot{a}_0}{\Omega} \right] \left(\frac{p}{\Omega} \cos \beta_w \right. \right. \\
&\quad \left. \left. + \frac{q}{\Omega} \sin \beta_w \right) + 4 \frac{a_0}{\Omega} \left(\frac{\dot{b}_1}{\Omega} - a_1 \right) \left(\frac{1}{3} - \epsilon + \epsilon^2 \right) \right\} + \frac{\mu}{4} \left\{ \epsilon (1 - \epsilon) \left[a_1 \left(\frac{\dot{b}_1}{\Omega} - a_1 \right) \right. \right. \\
&\quad \left. \left. + b_1 \left(\frac{\dot{a}_1}{\Omega} + b_1 \right) \right] + \frac{1}{4} (1 - \epsilon)^2 \left[b_1 \left(\frac{\dot{a}_1}{\Omega} + b_1 \right) + a_1 \left(\frac{\dot{b}_1}{\Omega} - a_1 \right) \right] \right. \\
&\quad \left. - \frac{1}{2} (1 - \epsilon^2) \left[a_1 \left(\frac{\dot{b}_1}{\Omega} - a_1 \right) + b_1 \left(\frac{\dot{a}_1}{\Omega} + b_1 \right) - 2a_0^2 - \frac{b_1^2}{2} - \frac{3}{2} a_1^2 \right] \right. \\
&\quad \left. - \frac{a_1}{4} (1 - \epsilon^2) \left(\frac{p}{\Omega} \cos \beta_w + \frac{q}{\Omega} \sin \beta_w \right) - \frac{b_1}{4} (1 - \epsilon^2) \left(-\frac{p}{\Omega} \sin \beta_w + \frac{q}{\Omega} \cos \beta_w \right) \right\} \\
&\quad - \frac{1}{8} \theta_t \lambda_2 - \frac{1}{6} (\theta_0 - K_1 a_0) \lambda_2 + (A_{1c} - K_1 a_1) \left[\frac{\mu}{16} (1 - \epsilon^2) \right] \lambda_1 \\
&\quad + (B_{1c} - K_1 b_1) \left[\frac{3}{16} \mu (1 - \epsilon^2) \right] \lambda_2 - \frac{\mu}{16} (1 - \epsilon^2) (\lambda_1 b_1 + \lambda_2 a_1) \\
&\quad - \frac{1}{2} (1 - \epsilon^2) \lambda_0 \lambda_2 - \frac{1}{6} \lambda_1 a_0 + \left(\frac{1}{3} - \frac{\epsilon}{2} \right) \lambda_2 \frac{\dot{a}_0}{\Omega}
\end{aligned}$$

FIGURE 2. MAIN ROTOR FORCES AND MOMENTS (CONT)

$$\begin{aligned}
\left(\frac{2C_Y}{a\sigma}\right)_w = & -\frac{1}{4} (\theta_0 - K_1 a_0) \left\{ \left[\left(\epsilon - \frac{2}{3} \right) \left(\frac{\dot{a}_1}{\Omega} + b_1 \right) - \frac{2}{3} b_1 \right] + 3a_0(1 - \epsilon^2)\mu - 2b_1(1 - \epsilon)\mu^2 \right. \\
& - \frac{2}{3} \left(-\frac{p}{\Omega} \sin \beta_w + \frac{q}{\Omega} \cos \beta_w \right) \left. \right\} - \frac{\theta_t}{4} \left\{ \left[\left(\frac{2\epsilon}{3} - \frac{1}{2} \right) \left(\frac{\dot{a}_1}{\Omega} + b_1 \right) - \frac{b_1}{2} \right] \right. \\
& + 2a_0\mu - b_1(1 - \epsilon^2)\mu^2 - \frac{1}{2} \left(-\frac{p}{\Omega} \sin \beta_w + \frac{q}{\Omega} \cos \beta_w \right) \left. \right\} \\
& - \frac{1}{4} (A_{1c} - K_1 a_1) \left\{ \left[\left(\epsilon - \frac{2}{3} \right) \frac{\dot{a}_0}{\Omega} + \lambda_0(1 - \epsilon^2) \right] + \mu \left[\frac{5a_1}{4} (1 - \epsilon^2) \right. \right. \\
& + \frac{1}{4} (1 - \epsilon)^2 \left(\frac{\dot{b}_1}{\Omega} - a_1 \right) \left. \right] + \frac{\mu}{4} (1 - \epsilon^2) \left(\frac{p}{\Omega} \cos \beta_w + \frac{q}{\Omega} \sin \beta_w \right) \left. \right\} \\
& - \frac{1}{4} (B_{1c} - K_1 b_1) \left\{ -\frac{2}{3} a_0 + \mu \left[\frac{7}{4} b_1(1 - \epsilon^2) + \frac{1}{4} (1 - \epsilon)^2 \left(\frac{\dot{a}_1}{\Omega} + b_1 \right) \right. \right. \\
& + \frac{1}{4} \left(-\frac{p}{\Omega} \sin \beta_w + \frac{q}{\Omega} \cos \beta_w \right) \left. \right] - \mu^2 [2a_0(1 - \epsilon)] \left. \right\} \\
& - \frac{1}{4} \left\{ 4 \left(\frac{1}{3} - \epsilon + \epsilon^2 \right) \frac{\dot{a}_0}{\Omega} \left(\frac{\dot{a}_1}{\Omega} + b_1 \right) - 2\lambda_0(1 - \epsilon)^2 \left(\frac{\dot{a}_1}{\Omega} + b_1 \right) \right. \\
& + \frac{2a_0}{3} \left(\frac{p}{\Omega} \cos \beta_w + \frac{q}{\Omega} \sin \beta_w \right) + 2a_0 \left(\frac{1}{3} - \frac{\epsilon}{2} \right) \left(\frac{\dot{b}_1}{\Omega} - a_1 \right) - 2b_1 \left[\frac{\lambda_0}{2} (1 - \epsilon^2) \right. \\
& - \frac{\dot{a}_0}{\Omega} \left(\frac{1}{3} - \frac{\epsilon}{2} \right) \left. \right] + \left[4 \left(\frac{1}{3} - \frac{\epsilon}{2} \right) \frac{\dot{a}_0}{\Omega} - 2(1 - \epsilon^2)\lambda_0 \right] \left(-\frac{p}{\Omega} \sin \beta_w + \frac{q}{\Omega} \cos \beta_w \right) \left. \right\} \\
& - \frac{\mu}{4} \left[6a_0\lambda_0(1 - \epsilon) - \frac{a_1 b_1}{2} (1 - \epsilon^2) - 3(1 - \epsilon)^2 a_0 \frac{\dot{a}_0}{\Omega} \right. \\
& - \frac{7}{4} (1 - \epsilon)^2 a_1 \left(\frac{\dot{a}_1}{\Omega} + b_1 \right) - \frac{5}{4} b_1(1 - \epsilon^2) \left(\frac{p}{\Omega} \cos \beta_w + \frac{q}{\Omega} \sin \beta_w \right) \\
& - \frac{7}{4} a_1(1 - \epsilon^2) \left(-\frac{p}{\Omega} \sin \beta_w + \frac{q}{\Omega} \cos \beta_w \right) - \frac{5}{4} (1 - \epsilon)^2 b_1 \left(\frac{\dot{b}_1}{\Omega} - a_1 \right) \left. \right] \\
& - \mu^2 [a_0 a_1 (1 - \epsilon)] + \frac{1}{8} \theta_t \lambda_1 + \frac{1}{6} (\theta_0 - K_1 a_0) \lambda_1 \\
& - \frac{(B_{1c} - K_1 b_1) \left[\frac{\mu}{16} (1 - \epsilon^2) \right] \lambda_1 - (A_{1c} - K_1 a_1) \left[\frac{\mu}{16} (1 - \epsilon^2) \right] \lambda_2}{+ \frac{1}{2} (1 - \epsilon^2) \lambda_0 \lambda_1 + \frac{7}{16} \mu (1 - \epsilon^2) \lambda_1 a_1 - \frac{1}{6} \lambda_2 a_0} \\
& - \frac{\left(\frac{1}{3} - \frac{\epsilon}{2} \right) \lambda_1 \frac{\dot{a}_0}{\Omega} + \frac{5}{16} \mu (1 - \epsilon^2) \lambda_2 b_1}{+ \frac{1}{2} (1 - \epsilon^2) \lambda_0 \lambda_1 + \frac{7}{16} \mu (1 - \epsilon^2) \lambda_1 a_1 - \frac{1}{6} \lambda_2 a_0}
\end{aligned}$$

FIGURE 2. MAIN ROTOR FORCES AND MOMENTS (CONT)

Main Rotor Hub Moments

The expressions for the main rotor hub moments are:

$$M_{HF} = (M_H)_w \cos \beta_w + (L_H)_w \sin \beta_w$$

$$L_{HF} = -(M_H)_w \sin \beta_w + (L_H)_w \cos \beta_w$$

where

$$(M_H)_w = \frac{N}{2} \left[K_\beta a_1 - eM_\beta (\ddot{a}_1 + 2\dot{b}_1\Omega - a_1\Omega^2) \right] - \frac{N}{2} I_\beta \Omega^2 \gamma \epsilon \left\{ -\left[\frac{1}{6} + \frac{\mu^2}{8} (1 - \epsilon) \right] \right. \\ \times (A_{1c} - K_1 a_1) - \frac{\mu}{4} (1 - \epsilon^2) a_0 + \frac{\mu^2}{8} (1 - \epsilon) b_1 + \left(\frac{1}{6} - \frac{\epsilon}{4} \right) \left(\frac{\dot{a}_1}{\Omega} + b_1 \right) \\ \left. + \frac{1}{6} \left(-\frac{p}{\Omega} \sin \beta_w + \frac{q}{\Omega} \cos \beta_w \right) + \frac{1}{6} \lambda_1 \right\}$$

and

$$(L_H)_w = \frac{N}{2} \left[K_\beta b_1 - eM_\beta (\ddot{b}_1 - 2\dot{a}_1\Omega - b_1\Omega^2) \right] - \frac{N}{2} I_\beta \Omega^2 \gamma \epsilon \left\{ \frac{\mu}{2} (1 - \epsilon^2) (\theta_0 - K_1 a_0) \right. \\ - \left[\frac{1}{6} + \frac{3}{8} \mu^2 (1 - \epsilon) \right] (B_{1c} - K_1 b_1) + \frac{\mu}{3} \theta_t + \frac{\mu}{2} (1 - \epsilon) \lambda_0 + \frac{\mu^2}{8} (1 - \epsilon) a_1 \\ - \frac{\mu}{4} (1 - \epsilon)^2 \frac{\dot{a}_0}{\Omega} + \left(\frac{1}{6} - \frac{\epsilon}{4} \right) \left(\frac{\dot{b}_1}{\Omega} - a_1 \right) \\ \left. + \frac{1}{6} \left(\frac{p}{\Omega} \cos \beta_w + \frac{q}{\Omega} \sin \beta_w \right) + \frac{1}{6} \lambda_2 \right\}$$

FIGURE 2. MAIN ROTOR FORCES AND MOMENTS (CONT)

Main Rotor Torque

The expressions for the main rotor torque are:

$$\begin{aligned}
 Q_F &= \frac{N}{2} \rho a c R^2 (\Omega R)^2 \frac{2C_Q}{a\sigma} \\
 \frac{2C_Q}{a\sigma} &= \frac{\delta}{4a} [1 + (1 - \epsilon^2)\mu^2] - (\theta_0 - K_1 a_0) \left[\frac{\lambda_0}{3} + \left(\frac{\epsilon}{3} - \frac{1}{4} \right) \frac{\dot{a}_0}{\Omega} + \frac{\mu}{6} \left(\frac{\dot{b}_1}{\Omega} \right) \right. \\
 &\quad \left. - \frac{\mu\epsilon}{4} \left(\frac{\dot{b}_1}{\Omega} - a_1 \right) + \frac{\mu}{6} \left(\frac{p}{\Omega} \cos \beta_w + \frac{q}{\Omega} \sin \beta_w \right) \right] + (A_{1c} - K_1 a_1) \left[\left(\frac{1}{8} - \frac{\epsilon}{6} \right) \left(\frac{\dot{a}_1}{\Omega} + b_1 \right) \right. \\
 &\quad \left. - \frac{\mu}{6} a_0 + \frac{b_1}{16} (1 - \epsilon^2)\mu^2 + \frac{1}{8} \left(-\frac{p}{\Omega} \sin \beta_w + \frac{q}{\Omega} \cos \beta_w \right) \right] \\
 &\quad + (B_{1c} - K_1 b_1) \left[\left(\frac{1}{8} - \frac{\epsilon}{6} \right) \left(\frac{\dot{b}_1}{\Omega} - a_1 \right) + \left(\frac{\epsilon}{4} - \frac{1}{6} \right) \mu \frac{\dot{a}_0}{\Omega} + \frac{1}{2} (1 - \epsilon^2) \left(\frac{\mu\lambda_0}{2} + \frac{a_1}{8} \mu^2 \right) \right. \\
 &\quad \left. + \frac{1}{8} \left(\frac{p}{\Omega} \cos \beta_w + \frac{q}{\Omega} \sin \beta_w \right) \right] - \theta_t \left[\frac{\lambda_0}{4} + \left(\frac{\epsilon}{4} - \frac{1}{5} \right) \frac{\dot{a}_0}{\Omega} + \frac{\mu}{8} \left(\frac{\dot{b}_1}{\Omega} \right) - \frac{\epsilon\mu}{6} \left(\frac{\dot{b}_1}{\Omega} - a_1 \right) \right] \\
 &\quad - \frac{1}{2} (1 - \epsilon^2) \left\{ \lambda_0^2 + \lambda_0 \mu a_1 + 2\lambda_0 \epsilon \frac{\dot{a}_0}{\Omega} + \mu \epsilon \left[a_1 \frac{\dot{a}_0}{\Omega} + a_0 \left(\frac{\dot{a}_1}{\Omega} + b_1 \right) \right] \right. \\
 &\quad \left. + \mu^2 \left(\frac{a_0^2}{2} + \frac{3}{8} a_1^2 + \frac{1}{8} b_1^2 \right) \right\} + \frac{\mu}{3} \left[a_1 \left(\frac{\dot{a}_0}{\Omega} \right) + a_0 \left(\frac{\dot{a}_1}{\Omega} + b_1 \right) \right] + \frac{2}{3} \lambda_0 \left(\frac{\dot{a}_0}{\Omega} \right) \\
 &\quad - \left[-\frac{\mu}{3} a_0 + \left(\frac{1}{4} - \frac{\epsilon}{3} \right) \left(\frac{\dot{a}_1}{\Omega} + b_1 \right) \right] \left(-\frac{p}{\Omega} \sin \beta_w + \frac{q}{\Omega} \cos \beta_w \right) \\
 &\quad - \left(\frac{1}{4} - \frac{\epsilon}{3} \right) \left(\frac{\dot{b}_1}{\Omega} - a_1 \right) \left(\frac{p}{\Omega} \cos \beta_w + \frac{q}{\Omega} \sin \beta_w \right) - \frac{1}{8} \left(-\frac{p}{\Omega} \sin \beta_w + \frac{q}{\Omega} \cos \beta_w \right)^2 \\
 &\quad - \frac{1}{8} \left(\frac{p}{\Omega} \cos \beta_w + \frac{q}{\Omega} \sin \beta_w \right)^2 - \left(\frac{1}{4} - \frac{2}{3} \epsilon + \frac{\epsilon^2}{2} \right) \left\{ \left(\frac{\dot{a}_0}{\Omega} \right)^2 \right. \\
 &\quad \left. + \frac{1}{2} \left[\left(\frac{\dot{a}_1}{\Omega} + b_1 \right)^2 + \left(\frac{\dot{b}_1}{\Omega} - a_1 \right)^2 \right] \right\} - \frac{\mu}{8} \theta_t \lambda_2 + \frac{\mu}{3} a_0 \lambda_1 \\
 &\quad - \frac{1}{8} (\lambda_1^2 + \lambda_2^2) - \left(\frac{1}{4} - \frac{\epsilon}{3} \right) \left(\frac{\dot{b}_1}{\Omega} - a_1 \right) \lambda_2 - \left(\frac{1}{4} - \frac{\epsilon}{3} \right) \left(\frac{\dot{a}_1}{\Omega} + b_1 \right) \lambda_1 \\
 &\quad - \frac{\mu}{6} (\theta_0 - K_1 a_0) \lambda_2 + \frac{1}{8} (A_{1c} - K_1 a_1) \lambda_1 + \frac{1}{8} (B_{1c} - K_1 b_1) \lambda_2 \\
 &\quad + \frac{\lambda_1}{4} \left(-\frac{p}{\Omega} \sin \beta_w + \frac{q}{\Omega} \cos \beta_w \right) + \frac{\lambda_2}{4} \left(\frac{p}{\Omega} \cos \beta_w + \frac{q}{\Omega} \sin \beta_w \right)
 \end{aligned}$$

FIGURE 2. MAIN ROTOR FORCES AND MOMENTS (CONT)

A second set of equations was formed by replacing the torque equation with the coning equation. Obviously, this set yields a consistent set of answers for a_0 , a_1 , b_1 , λ_0 , λ_1 , and λ_2 under the above defined consistency test. These equations rearranged in the form used for solving for the flapping and inflow coefficients are shown in figure 3.

Once the set of equations was chosen, and the wind tunnel data from Reference 2 processed through them, the values of λ_0 , λ_1 , and λ_2 were known for each trim condition. The procedure just described and the set of test conditions used are summarized in Figures 4 and 5 respectively. The wind tunnel configuration and the wind tunnel data used in this analysis are tabulated in the appendix.

The effects on inflow values of angle of attack, rotor height above the ground, and rotor disc loading were sought. Each set of parameters shown in Figure 5 represents a speed sweep at these values. The matrix of test conditions was not all inclusive. For instance, the runs which were used to define the effect of ground proximity were done only at one angle of attack and disc loading. Likewise, the runs to define angle of attack effects were done at only one rotor height. Therefore, a set of parameter values were chosen as the nominal configuration and incremental changes used to define the results for any other configuration. The nominal configuration was chosen as:

Disc Loading (DL)	=	8 PSF
Angle of Attack (α)	=	1. DEG
Ground Proximity (h/d)	=	0.4

In other words, to define the results for DL=8, $\alpha=6$ and h/d=1, the difference in results for DL=8, $\alpha=6$ and h/d=0.4 and DL=8, $\alpha=1$, h/d=0.4 would be added to the results at DL=8, $\alpha=1$, h/d=1. Using this approach, available data and trends were used to complete the matrix over the parameter ranges of interest.

The effect of ground proximity is shown in Figures 6, 7 and 8. The effect on steady induced downwash (inflow) is shown in Figure 6 for four

$P^2 + \frac{\gamma K_1 \mu^2}{4} \left(\frac{1}{2} - \varepsilon + \frac{\varepsilon^2}{2} \right)$	$-\frac{\gamma \mu}{4} \left(\frac{\varepsilon}{2} - \varepsilon^2 \right)$	$-\frac{\gamma K_1 \mu}{4} \left(\frac{2}{3} - \varepsilon \right)$	$-\frac{\gamma}{2} \left(\frac{1}{3} - \frac{\varepsilon}{2} \right)$	0 0	$-\frac{\gamma \mu}{8} \left(\frac{2}{3} - \varepsilon \right)$
$-\frac{\gamma \mu}{2} \left(\frac{1}{3} - \frac{\varepsilon}{2} \right)$	$P^2 - 1 + \frac{\gamma K_1 \mu^2}{8} \left(\frac{1}{2} - \varepsilon + \frac{\varepsilon^2}{2} \right)$	$\frac{\gamma}{2} \left(\frac{1}{4} - \frac{2}{3} \varepsilon + \frac{\varepsilon^2}{2} \right) + \frac{\gamma \mu^2}{8} \left(\frac{1}{2} - \varepsilon + \frac{\varepsilon^2}{2} \right)$	0 0	$\frac{\gamma}{2} \left(\frac{1}{4} - \frac{\varepsilon}{3} \right)$	0.0
$-\frac{\gamma K_1 \mu}{2} \left(\frac{2}{3} - \varepsilon \right)$	$-\frac{\gamma}{2} \left(\frac{1}{4} - \frac{2}{3} \varepsilon + \frac{\varepsilon^2}{2} \right) + \frac{\gamma \mu^2}{8} \left(\frac{1}{2} - \varepsilon + \frac{\varepsilon^2}{2} \right)$	$P^2 - 1 + \frac{3\gamma K_1 \mu^2}{8} \left(\frac{1}{2} - \varepsilon + \frac{\varepsilon^2}{2} \right)$	$\frac{\gamma \mu}{2} \left(\frac{1}{2} - \varepsilon + \frac{\varepsilon^2}{2} \right)$	0 0	$\frac{\gamma}{2} \left(\frac{1}{4} - \frac{\varepsilon}{3} \right)$
$-K_1 C_0 \left[\frac{1}{3} + \frac{\mu^2}{2} (1 - \varepsilon) \right]$	$\frac{C_0 \mu \varepsilon}{2} (1 - \varepsilon)$	$\frac{C_0 K_1 \mu}{2} (1 - \varepsilon^2)$	$\frac{1}{2} C_0 (1 - \varepsilon^2)$	0.0	$\frac{\mu}{4} C_0 (1 - \varepsilon^2)$
$\frac{C_0 \mu \varepsilon}{4} (1 - \varepsilon^2)$	$-C_0 \varepsilon \left[\frac{K_1}{6} + \frac{K_1 \mu^2}{8} (1 - \varepsilon) \right] + \frac{N}{2} \left(\frac{K_B}{\Omega^2} + eM_B \right)$	$-C_0 \varepsilon \left[\frac{\mu^2}{8} (1 - \varepsilon) + \left(\frac{1}{6} - \frac{\varepsilon}{4} \right) \right]$	0.0	$\frac{-C_0 \varepsilon}{6}$	0.0
$\frac{C_0 K_1 \mu \varepsilon}{2} (1 - \varepsilon^2)$	$-C_0 \varepsilon \left[\frac{\mu^2}{8} (1 - \varepsilon) - \left(\frac{1}{6} - \frac{\varepsilon}{4} \right) \right]$	$-C_0 \varepsilon \left[\frac{K_1}{6} + \frac{3K_1 \mu^2}{8} (1 - \varepsilon) \right] + \frac{N}{2} \left(\frac{K_B}{\Omega^2} + eM_B \right)$	$\frac{-C_0 \mu \varepsilon}{2} (1 - \varepsilon)$	0.0	$\frac{-C_0 \varepsilon}{6}$

\approx

$$C_0 = \frac{N}{2} I_{\beta} \gamma$$

FIGURE 3. EQUATIONS FOR THE SOLUTION OF FLAPPING AND INFLOW COEFFICIENTS

$$\vec{f} = \begin{bmatrix} \frac{\gamma}{2} \left[\left(\frac{1}{4} - \frac{\varepsilon}{3} \right) + \frac{\mu^2}{2} \left(\frac{1}{2} - \varepsilon + \frac{\varepsilon^2}{2} \right) \right] \theta_0 \\ + \frac{\gamma}{2} \left[\left(\frac{1}{3} - \frac{\varepsilon}{4} \right) + \frac{\mu^2}{2} \left(\frac{1}{3} - \frac{\varepsilon}{2} \right) \right] \theta_t \\ - \frac{\gamma \mu}{2} \left(\frac{1}{3} - \frac{\varepsilon}{2} \right) B_{1c} - \frac{M_B g}{I_B \Omega^2} \\ \hline \frac{\gamma}{2} \left[\left(\frac{1}{4} - \frac{\varepsilon}{3} \right) + \frac{\mu^2}{4} \left(\frac{1}{2} - \varepsilon + \frac{\varepsilon^2}{2} \right) \right] A_{1c} \\ \hline - \frac{\gamma \mu}{2} \left(\frac{2}{3} - \varepsilon \right) \theta_0 - \frac{\gamma \mu}{2} \left(\frac{1}{2} - \frac{2}{3} \varepsilon \right) \theta_t \\ + \frac{\gamma}{2} \left[\left(\frac{1}{4} - \frac{\varepsilon}{3} \right) + \frac{3\mu^2}{4} \left(\frac{1}{2} - \varepsilon + \frac{\varepsilon^2}{2} \right) \right] B_{1c} \\ \hline \frac{T_F R}{\Omega^2} - C_O \left[\frac{1}{3} + \frac{\mu^2}{2} (1 - \varepsilon) \right] \theta_0 \\ - C_O \left[\frac{1}{4} + \frac{\mu^2}{4} (1 - \varepsilon^2) \right] \theta_t + \frac{C_O \mu}{2} (1 - \varepsilon^2) B_{1c} \\ \hline \frac{M_{HF}}{\Omega^2} - C_O \varepsilon \left[\frac{1}{6} + \frac{\mu^2}{8} (1 - \varepsilon) \right] A_{1c} \\ \hline \frac{L_{HF}}{\Omega^2} + C_O \varepsilon \left[\frac{\mu}{2} (1 - \varepsilon^2) \right] \theta_0 \\ - C_O \varepsilon \left[\frac{1}{6} + \frac{3\mu^2}{8} (1 - \varepsilon) \right] B_{1c} + C_O \varepsilon \left(\frac{\mu}{3} \right) \theta_t \end{bmatrix}$$

$$A \vec{x} = \vec{f} \quad \vec{x}^T = (a_0 \ a_1 \ b_1 \ \lambda_0 \ \lambda_1 \ \lambda_2)$$

FIGURE 3. EQUATIONS FOR THE SOLUTION OF FLAPPING AND INFLOW COEFFICIENTS (CONTINUED)

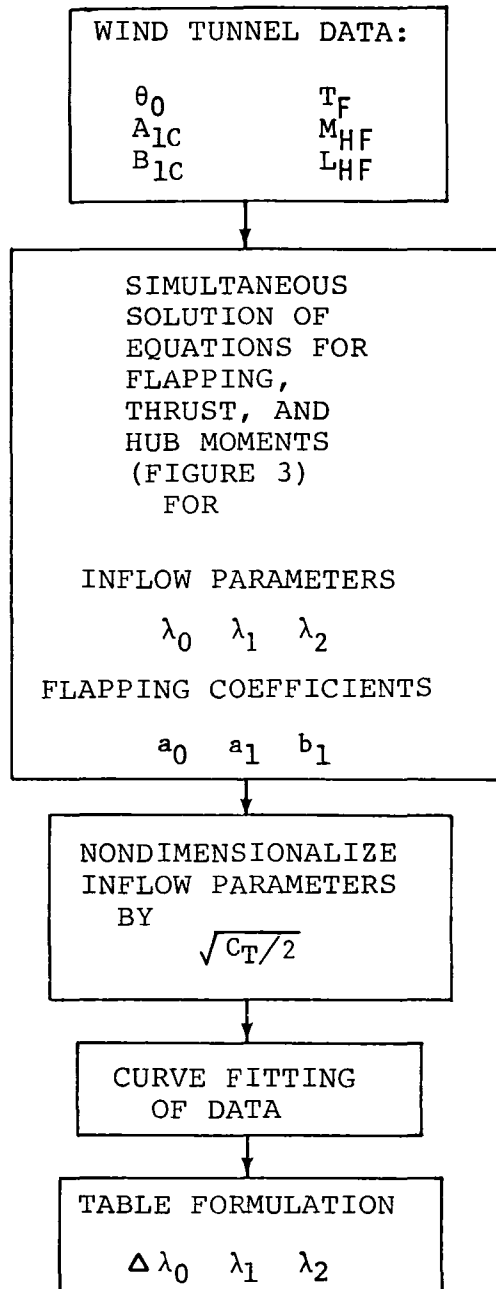


FIGURE 4. LOW SPEED, LOW ALTITUDE INFLOW DERIVATION SCHEME.

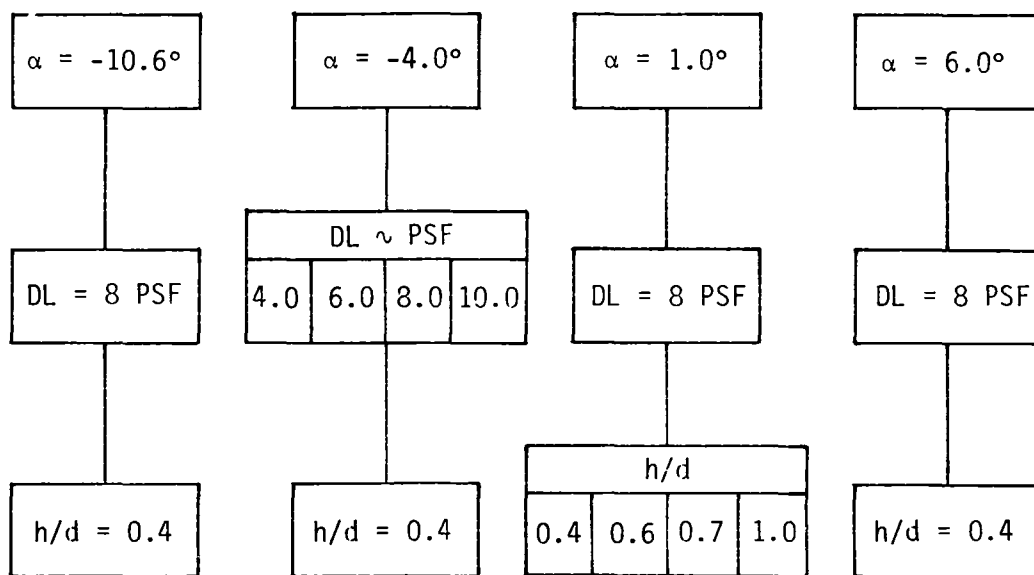


FIGURE 5. LOW SPEED, LOW ALTITUDE WIND TUNNEL TEST CONDITIONS.

$\psi = 0^\circ$
 $\alpha = 1^\circ$
DL = 8 PSF

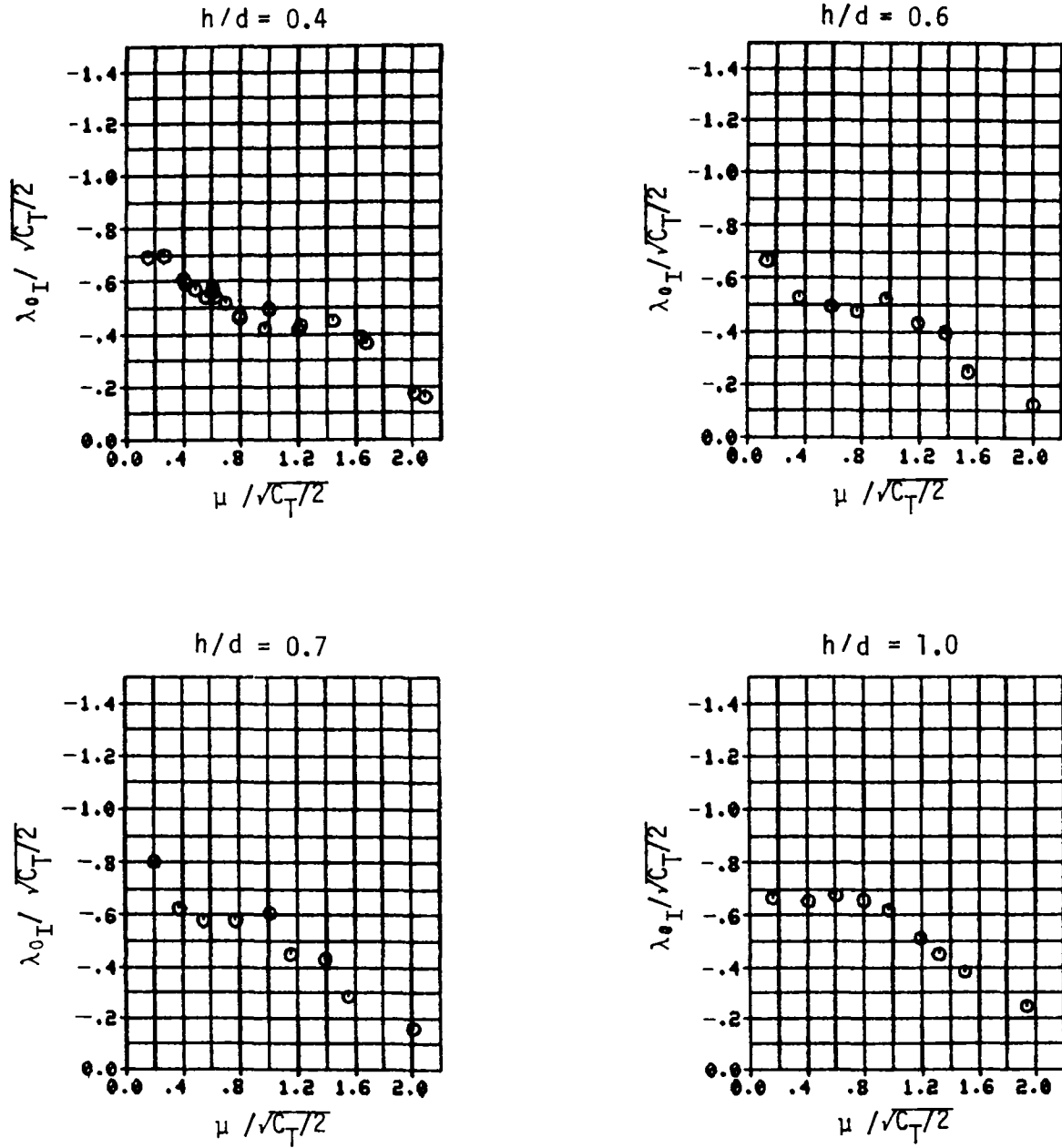


FIGURE 6. EFFECT OF GROUND PROXIMITY ON STEADY INDUCED INFLOW COEFFICIENT.

$\psi = 0^\circ$
 $\alpha = 1^\circ$
DL = 8 PSF

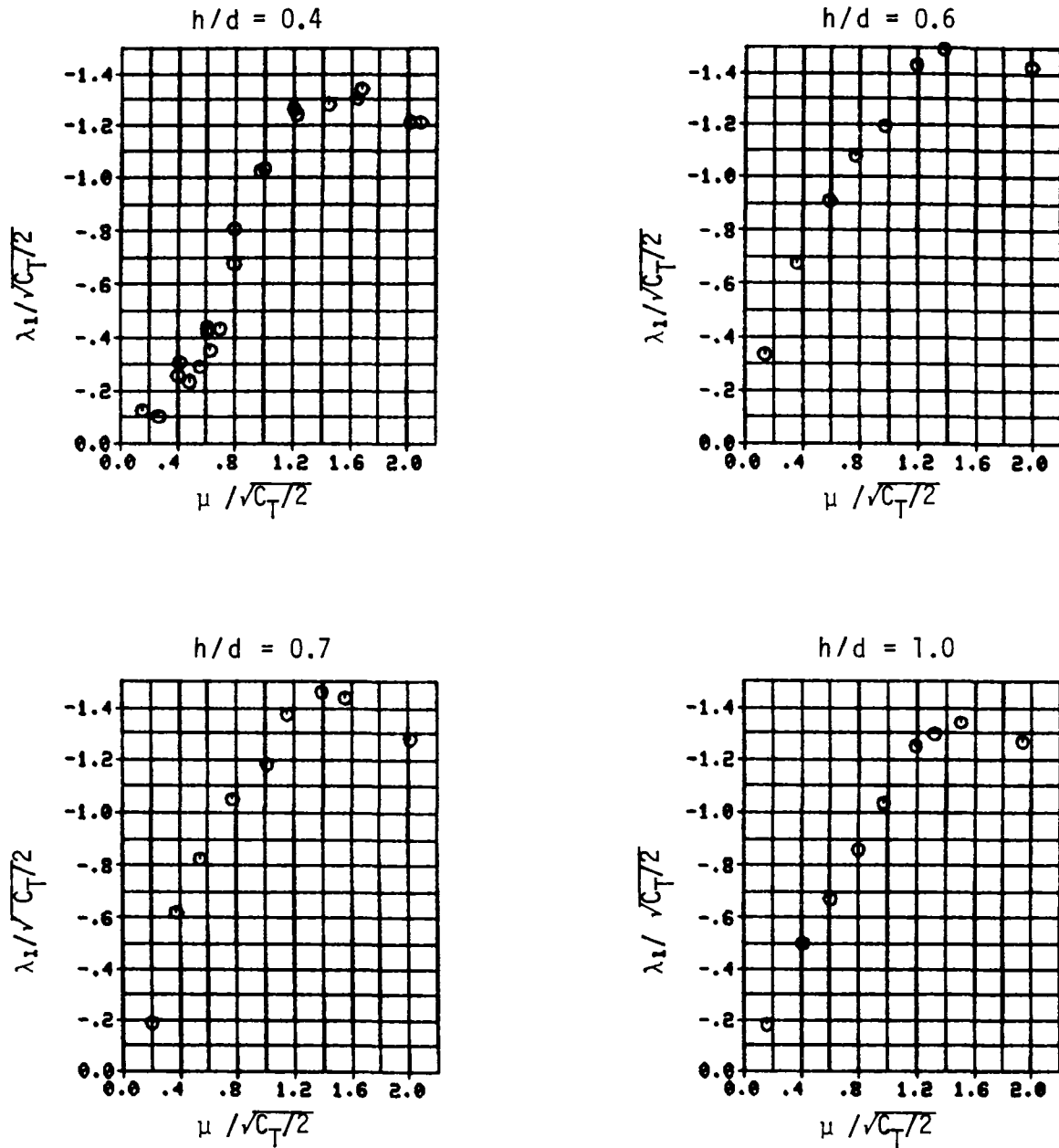


FIGURE 7. EFFECT OF GROUND PROXIMITY ON LONGITUDINAL INFLOW COEFFICIENT.

$\psi = 0^\circ$
 $\alpha = 1^\circ$
 DL = 8 PSF

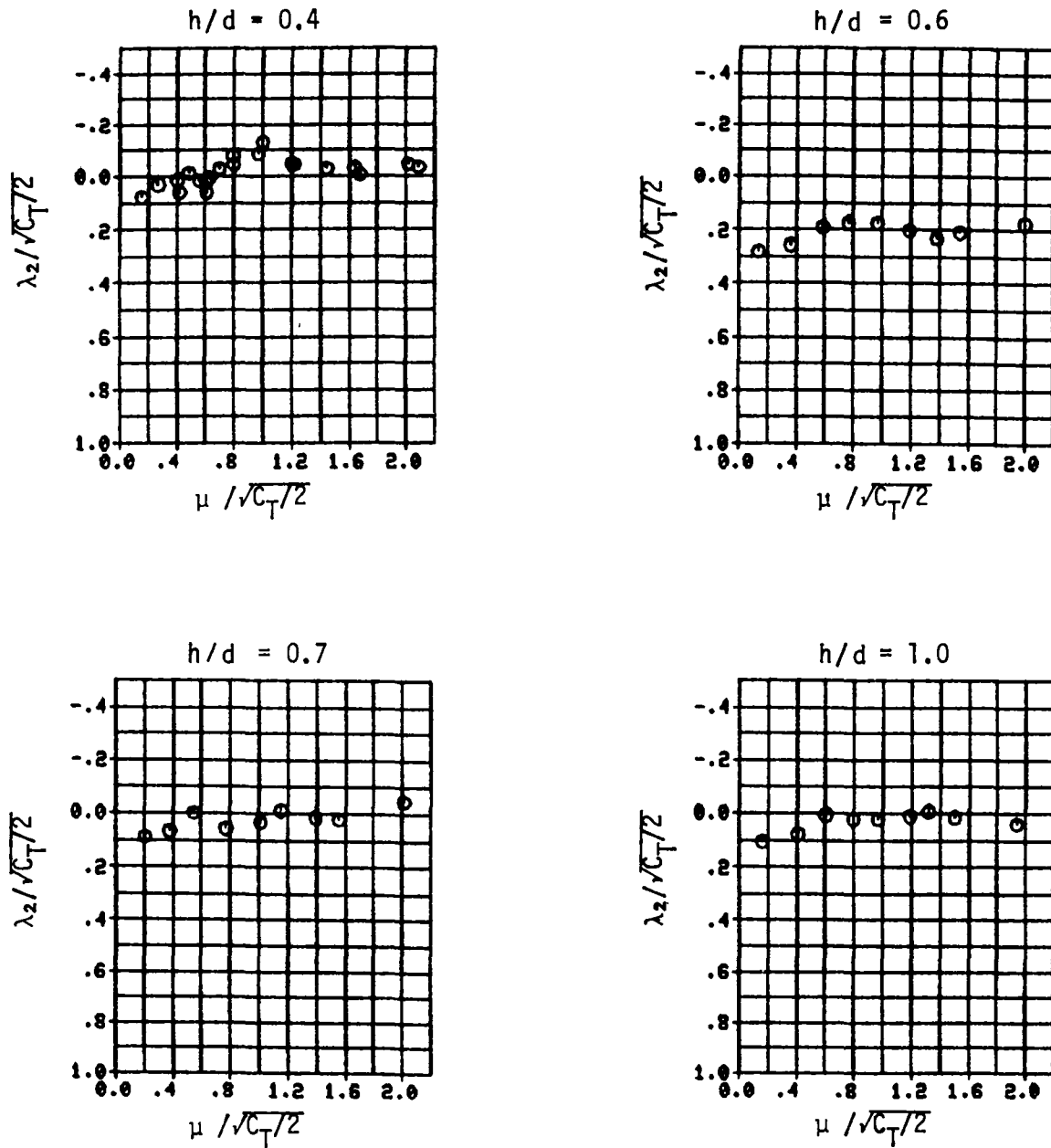


FIGURE 8. EFFECT OF GROUND PROXIMITY ON LATERAL INFLOW COEFFICIENT.

values of nondimensionalized rotor height (h/d). Note that steady induced inflow, rather than total uniform inflow, is plotted in Figure 6 and in subsequent similar plots. This value is obtained by removing the free-stream inflow component from the solution for λ_0 . The magnitude of λ_{0I} is generally reduced at lower speeds with decreasing rotor height. The shape of the longitudinal inflow coefficient (λ_1), as shown in Figure 7 for an $h/d=1$, is consistent with the simple analytical results of Reference 3. However, the peak value from Figure 7 is considerably higher than the peak analytical value in Reference 3. The delayed increase in λ_1 , with airspeed for an $h/d=0.4$ is consistent with the corresponding test data for lateral hub moment. The comparatively small values for the lateral inflow coefficient (λ_2), as shown in Figure 8, is consistent with previous assumptions (see References 3 and 6). The somewhat larger values for λ_2 for an $h/d=0.6$ is unexplained. There appears to be a bias value, possibly due to a bias in pitching hub moment in the test data. It is therefore concluded from this data that λ_2 can be neglected.

The effect of angle of attack is shown in Figures 9, 10 and 11. Figure 9 shows that the effect on λ_{0I} of varying angle of attack from -10.6 degrees to 6.0 degrees is small. On the other hand, λ_1 , as shown in Figure 10, shows a definite decrease in peak value with a decrease in angle of attack. And as before, λ_2 shows a scatter of data points about zero.

Finally, the effect of disc loading can be seen in Figures 12, 13 and 14. There appears from these plots to be little effect of disc loading on the nondimensionalized inflow coefficients. Since $\sqrt{C_T}/2$ was originally chosen as a parameter to nondimensionalize disc loading effects this result was expected and demonstrates the validity of the choice.

Steep Descent Effects

A method of calculating the main rotor inflow due to operation in vertical or near vertical descents was obtained from the experimental data presented in Reference 4. The author of Reference 4 used rotor thrust and power to calculate mean induced downwash at various angles of attack and descent rates. The angle of attack is measured relative to the hub disc plane and the descent rate is

$\psi = 0^\circ$
 $h/d = 0.4$
 $DL = 8 \text{ PSF}$

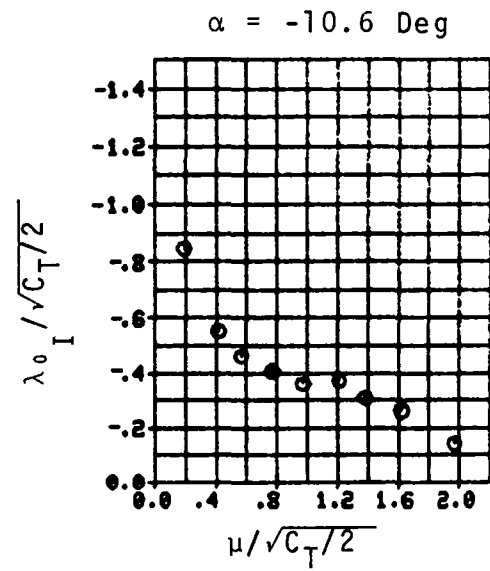
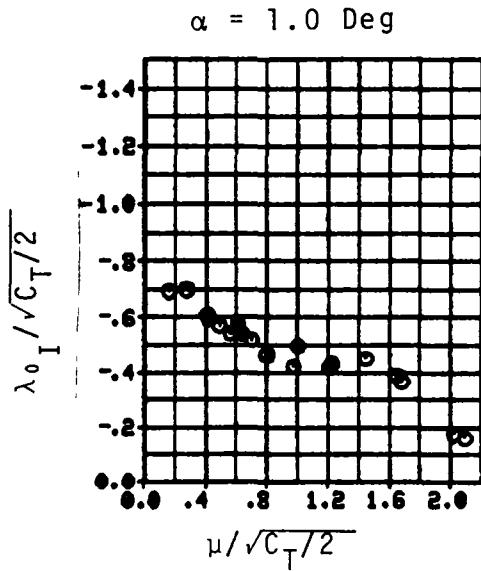
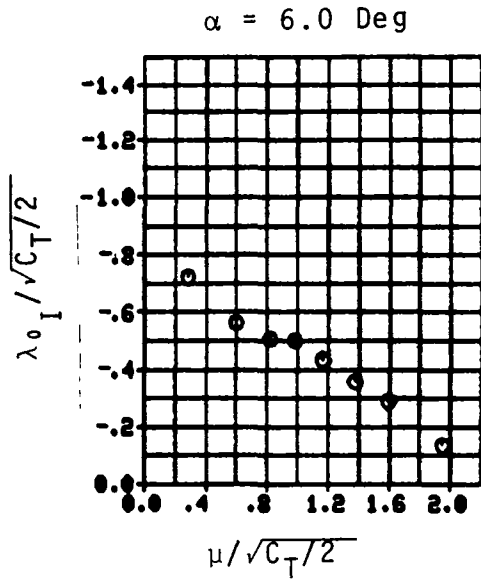


FIGURE 9. EFFECT OF ANGLE OF ATTACK ON THE STEADY INDUCED INFLOW COEFFICIENT.

$\psi = 0^\circ$
 $h/d = 0.4$
 $DL = 8 \text{ PSF}$

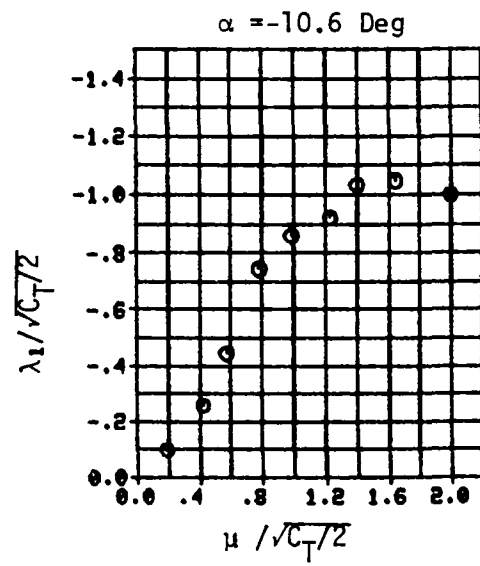
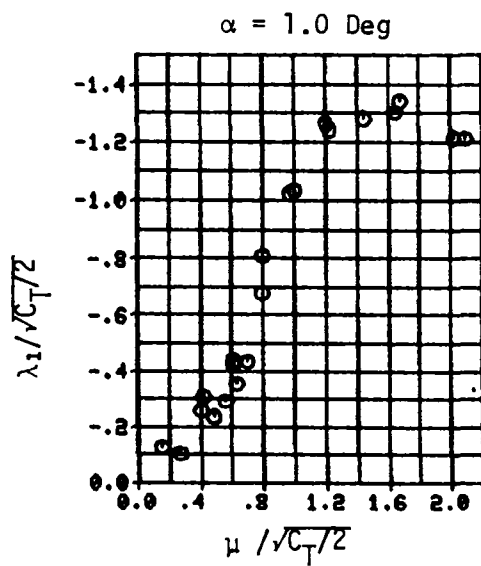
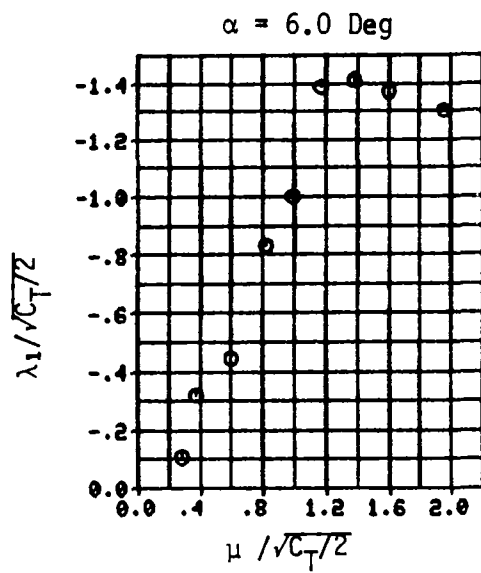


FIGURE 10. EFFECT OF ANGLE OF ATTACK ON THE LONGITUDINAL INFLOW COEFFICIENT.

$\psi = 0^\circ$
 $h/d = 0.4$
 $DL = 8 \text{ PSF}$

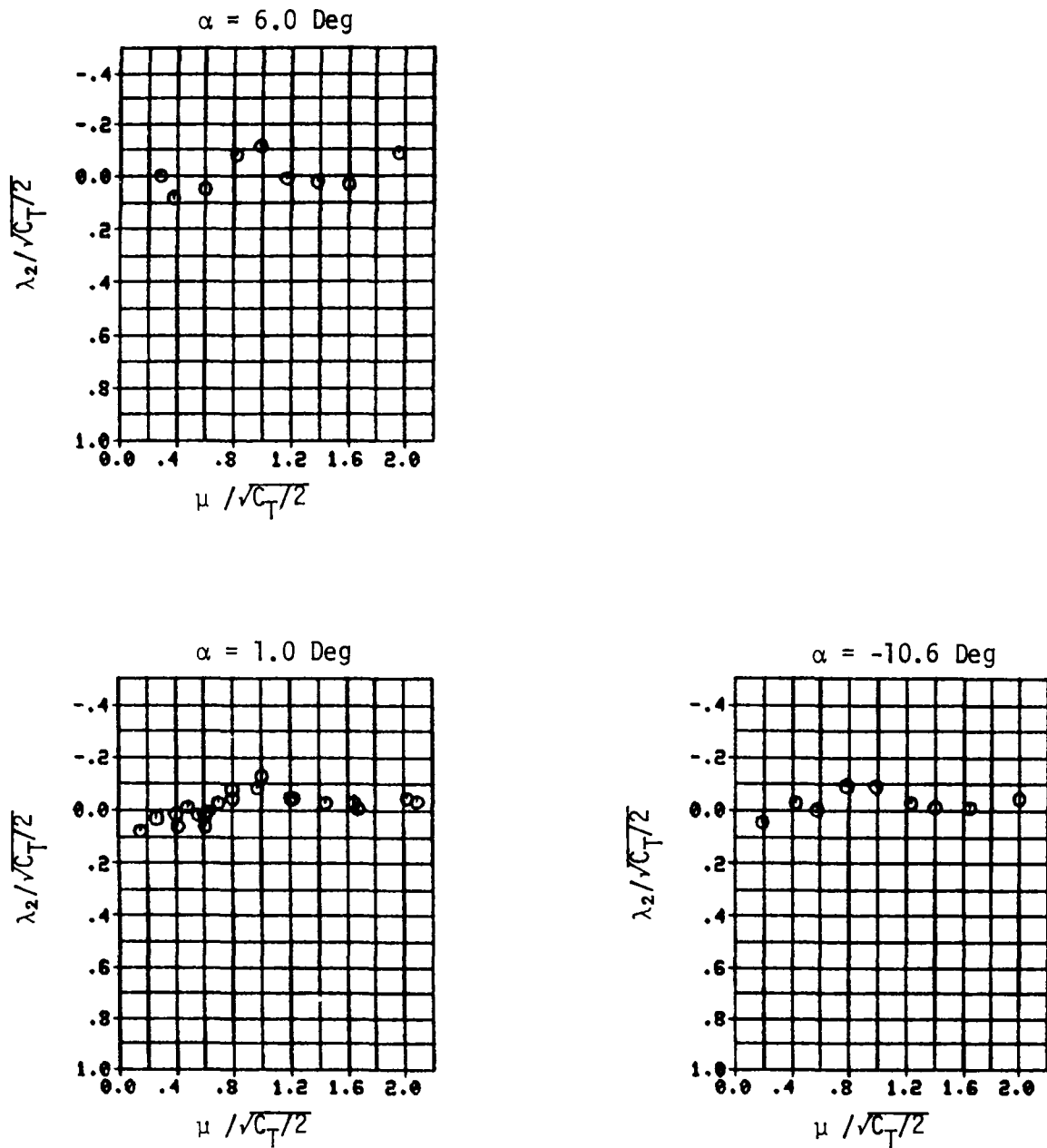


FIGURE 11. EFFECT OF ANGLE OF ATTACK ON THE LATERAL INFLOW COEFFICIENT.

$$\begin{aligned}\psi &= 0^\circ \\ \alpha &= -4^\circ \\ h/d &= 0.4\end{aligned}$$

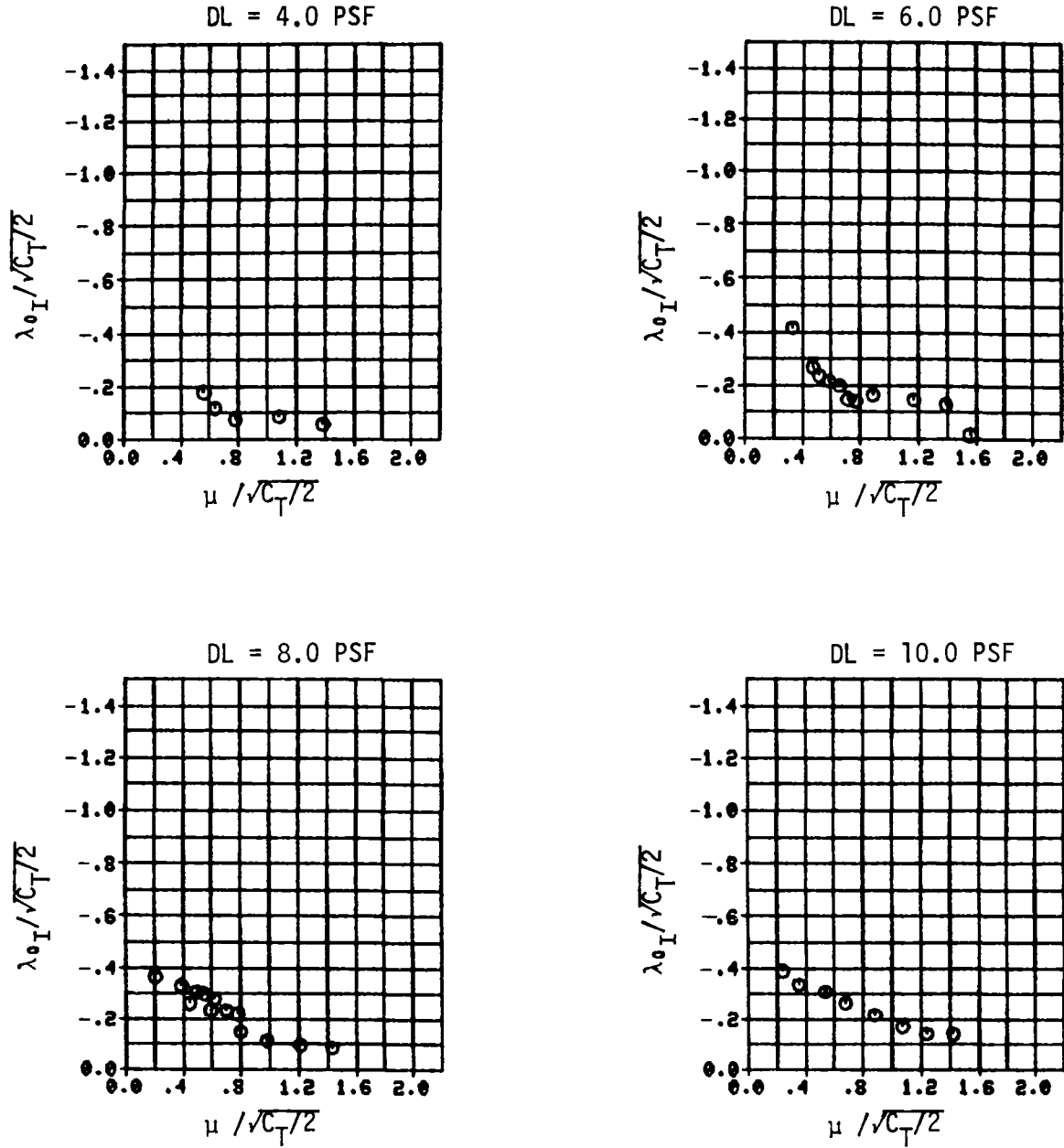


FIGURE 12. EFFECT OF DISC LOADING ON THE STEADY INDUCED INFLOW COEFFICIENT.

$$\begin{aligned}\psi &= 0^\circ \\ \alpha &= -4^\circ \\ h/d &= 0.4\end{aligned}$$

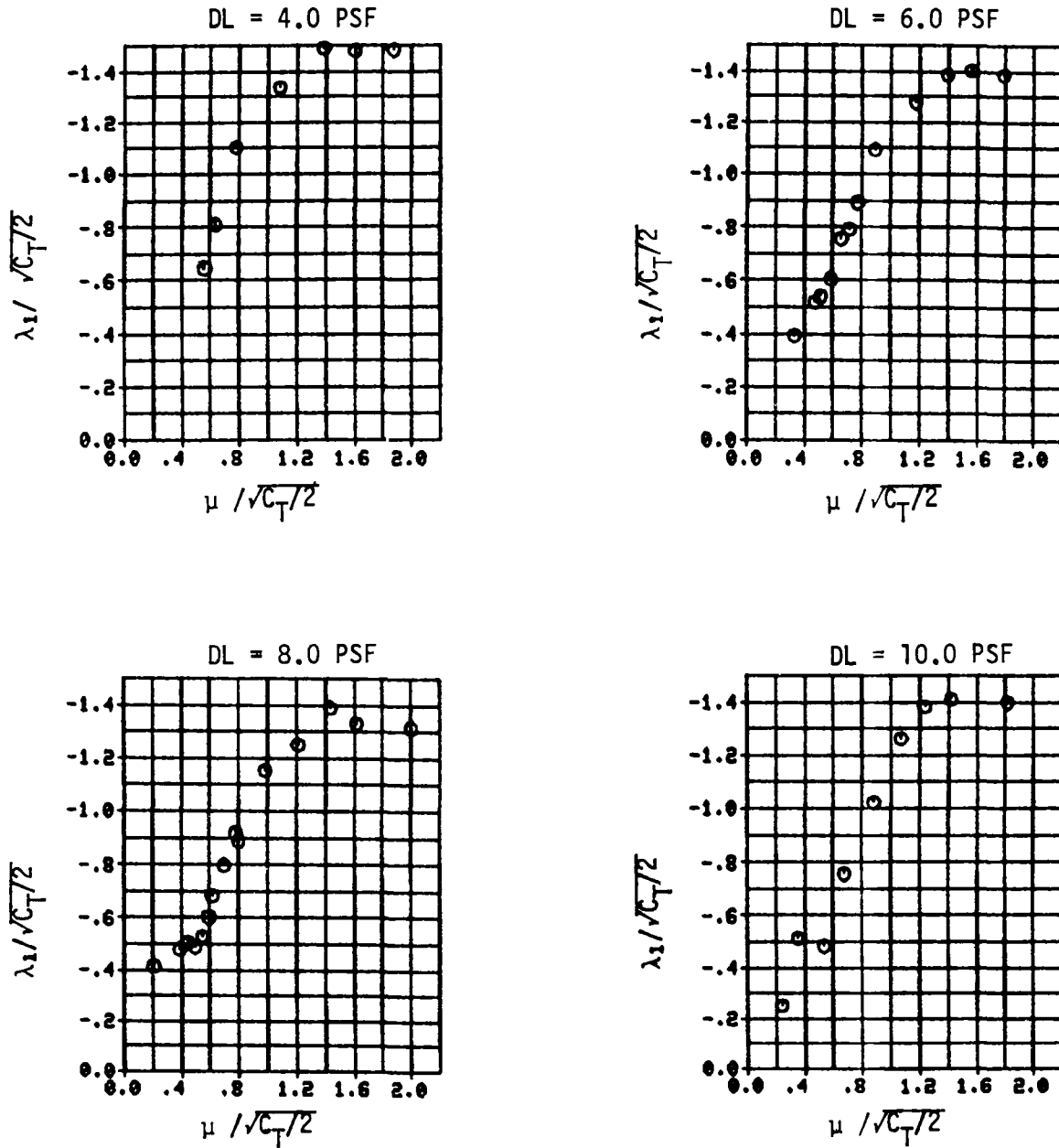


FIGURE 13. EFFECT OF DISC LOADING ON THE LONGITUDINAL INFLOW COEFFICIENT.

$\psi = 0^\circ$
 $\alpha = -4^\circ$
 $h/d = 0.4$

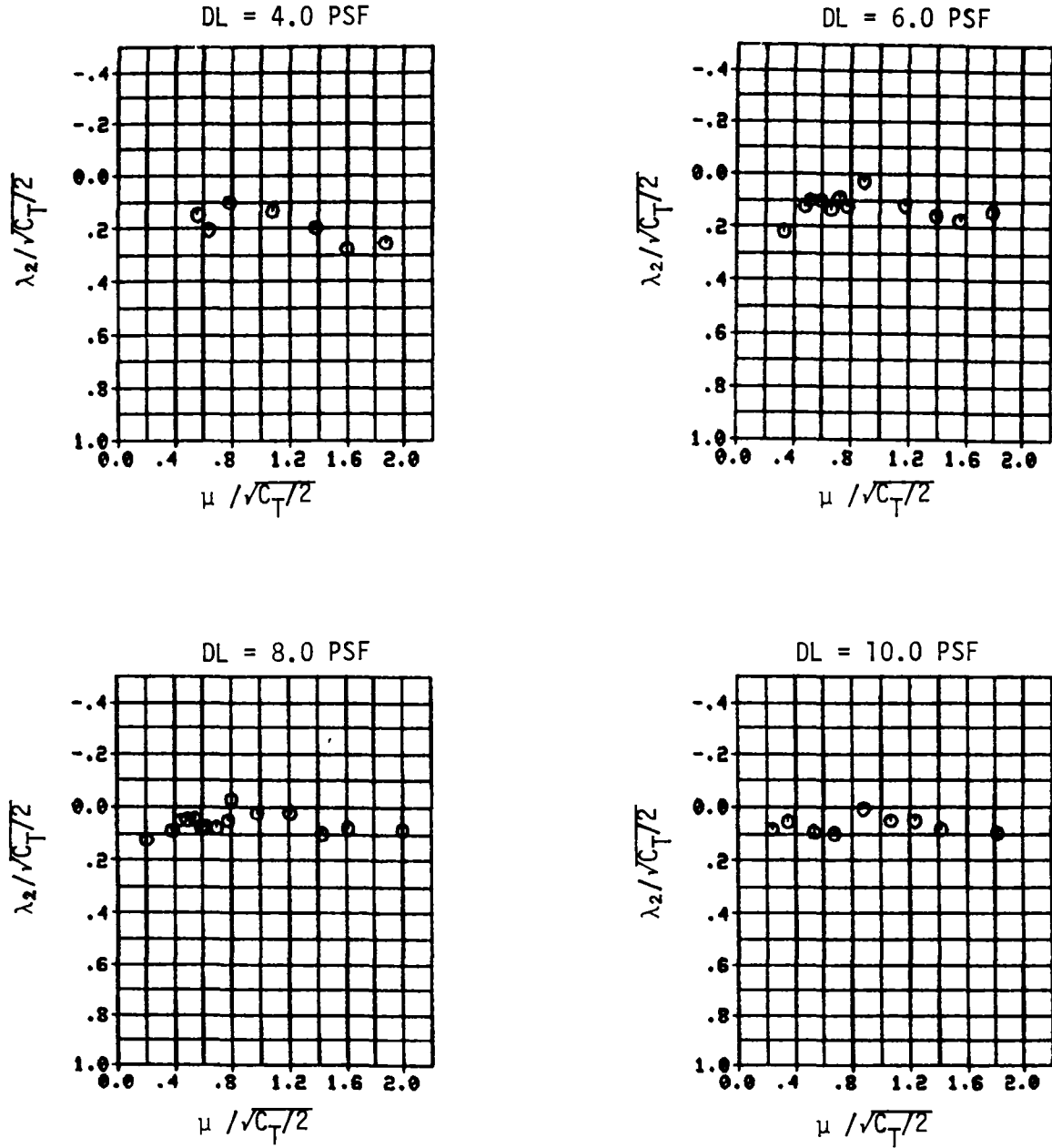


FIGURE 14. EFFECT OF DISC LOADING ON THE LATERAL INFLOW COEFFICIENT.

defined as the component of relative wind parallel to the shaft axis. The induced downwash and the rate of descent (R/D) are nondimensionalized by the mean hover induced downwash. This nondimensional induced downwash is plotted in Figure 15 as a function of angle of attack and nondimensional rate of descent. The dotted lines represent the results obtained when momentum theory is used.

For the present model, curves were faired through the experimental data to represent the mean experimental induced downwash. These curves were then faired into the momentum curves at hover and at very high rates of descent. The curves were cross plotted and adjusted for observed trends. Values for intermediate angles of attack were generated and a complete set of curves formed.

The second part of the vortex-ring state that was modelled deals with thrust fluctuations. It was observed in reference 4 that thrust fluctuations were part of the unsteady nature of the vortex-ring state. Figure 16 shows a plot from reference 4 of the magnitude of the thrust fluctuations as a fraction of the mean rotor thrust. This data was replotted as a function of angle of attack and nondimensional rate of descent

The thrust fluctuations are introduced as a simple harmonic input to be added to the steady thrust as follows.

$$\Delta T = \left(\frac{\Delta T}{T_F} \right) T_F \sin \omega_v t$$

Unfortunately, the frequency (ω_v), or frequencies, are not well defined. The frequency data presented in Reference 4 is incomplete. Figure 17(a) shows a plot of how two periods associated with the thrust fluctuations from Reference 4 vary with nondimensional rate of descent. This is the only data of this kind presented and is for one angle of attack only. The periods shown in Figure 17(a) are not nondimensionalized and thus apply only to the test case. The periods were assumed to fit a hyperbola and therefore were converted to straight line frequency plots as shown in Figure 17(b). Based upon the observations noted in Reference 4, the frequency for any size rotor is calculated from the Karman vortex-shedding frequency formula

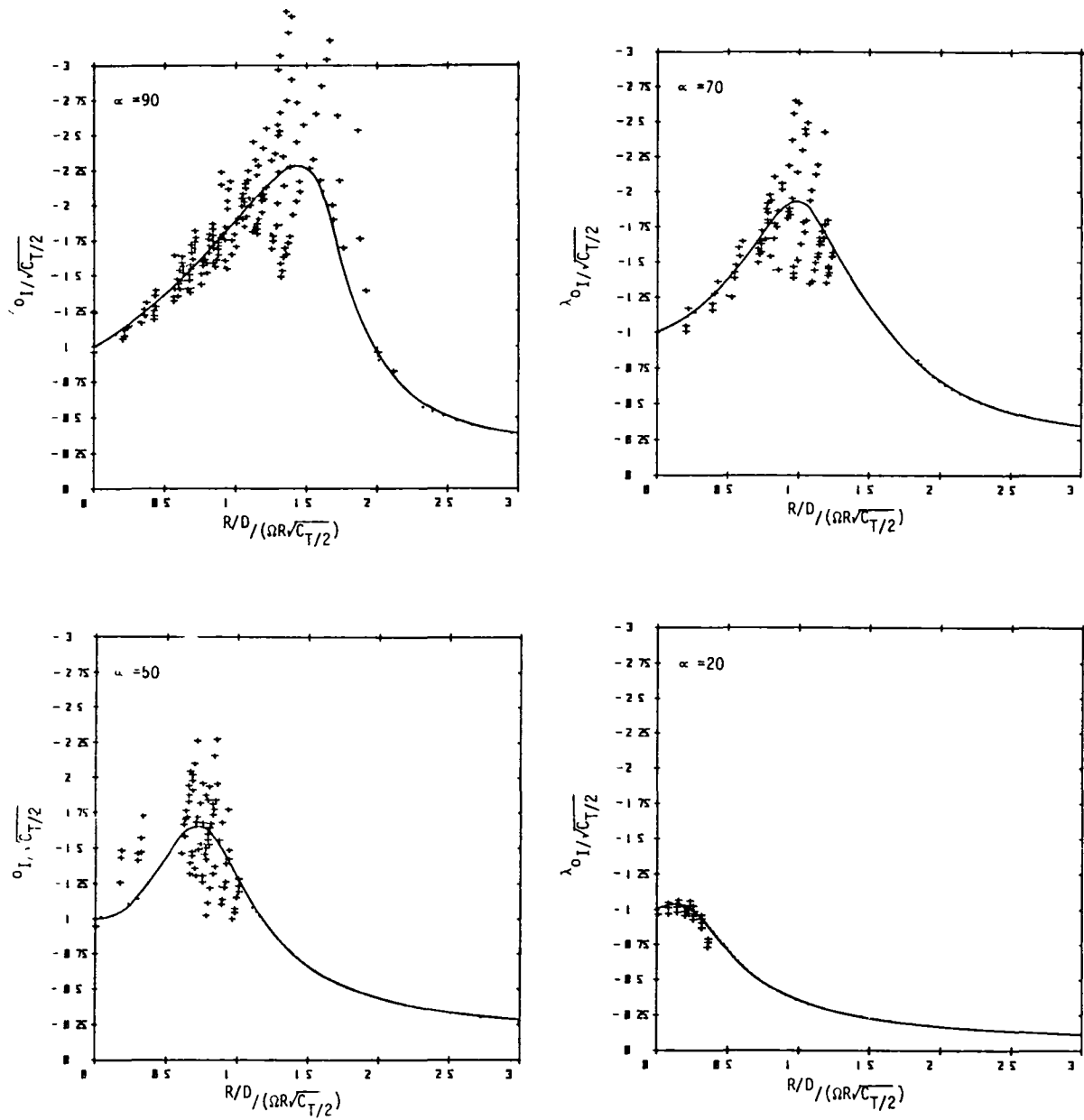


FIGURE 15. INDUCED VELOCITY PLOTS FROM REFERENCE 4.

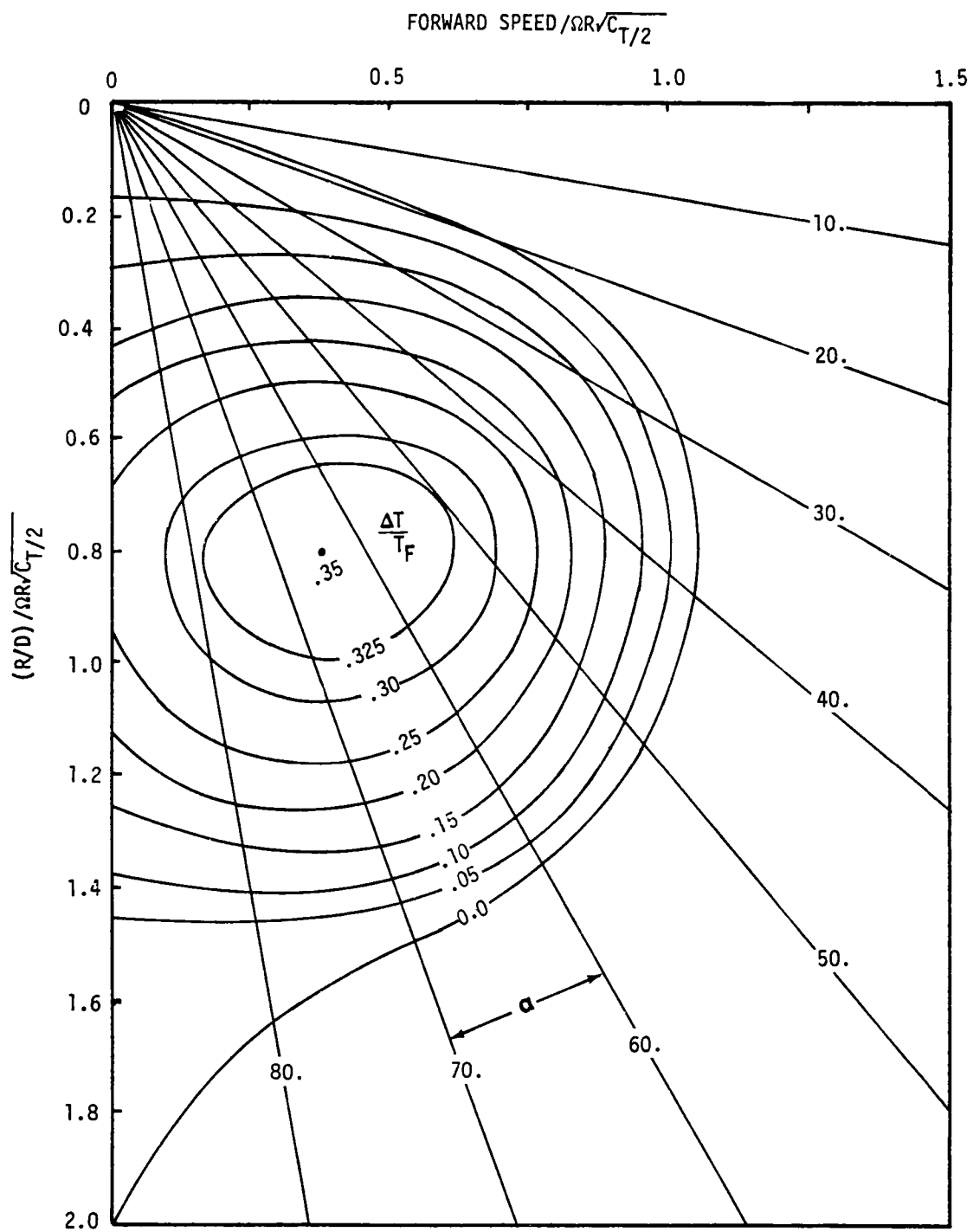


FIGURE 16. EXPANDED THRUST FLUCTUATION CURVES FROM REFERENCE 4.

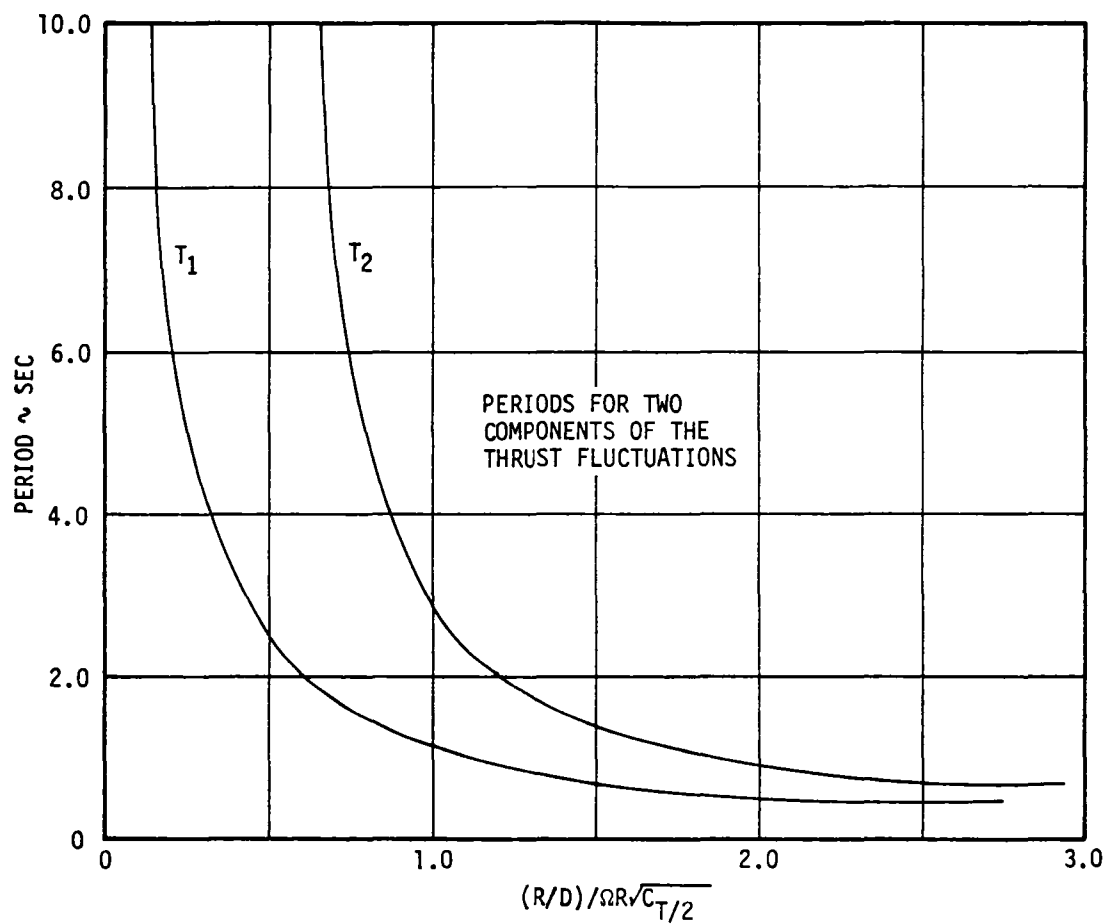


FIGURE 17a. PERIODICITY OF THRUST FLUCTUATIONS.

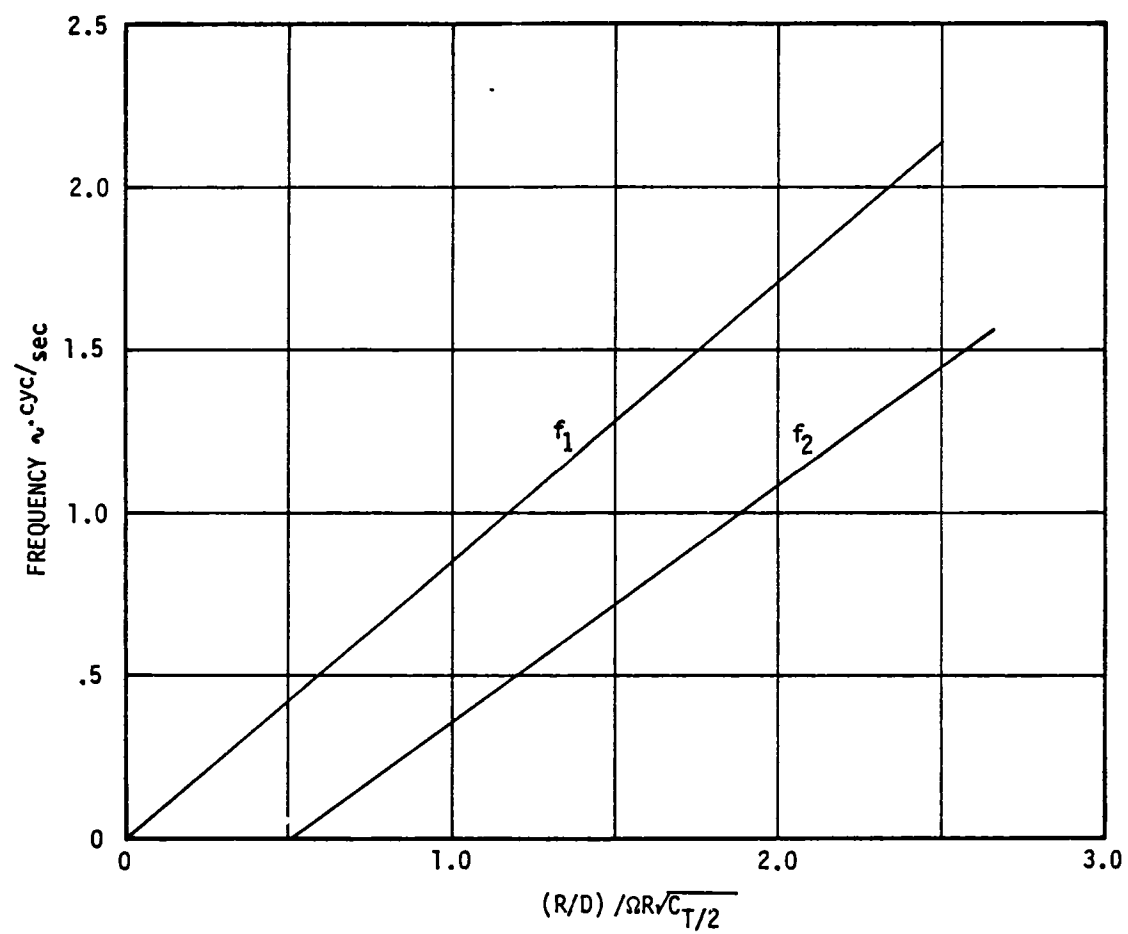


FIGURE 17b. PERIODICITY OF THRUST FLUCTUATIONS.

$$\omega_v = \frac{K_f V \sin \alpha}{d}, \quad \text{rad/sec}$$

The constant K_f is an approximation derived from the limited frequency data presented. This was done in the following way:

$$\begin{aligned} K_f &= \frac{\omega_v d}{V \sin \alpha} = \frac{\omega_v d}{R/D} \\ &= \frac{4\pi f_v}{\Omega \sqrt{C_T}/2} \frac{(\Omega R \sqrt{C_T}/2)}{R/D} \end{aligned}$$

Using this relationship and the curves from Figure 17, two values for K_f were calculated (1.1 and 2.3). Since the frequency data is sparse and the representation simple, the need to use two frequencies is questionable. Therefore, a single value for K_f of 2 is recommended. Thus the total thrust is defined as:

$$T = T_F \left(1 + \frac{\Delta T}{T_F} \sin \omega_v t \right)$$

where T_F is mean thrust value from rotor thrust equation

$\frac{\Delta T}{T_F}$ is fractional value of thrust fluctuation

$$\omega_v = 2 \frac{V \sin \alpha}{d}$$

MODEL CHECKOUT

Model Implementation on Boeing Vertol Simulator

A schematic of the modifications as formulated for the Boeing Vertol simulator is presented in Figure 18. In order to allow these modifications to be engaged at all times during the simulations, flight conditions involving airspeeds and angles of attack beyond those values tested had to be considered. These conditions led to certain extensions to the data which will be described in the discussion that follows.

The first step in the procedure assumes that the uniform induced downwash from momentum theory has been calculated. The modifications then start with a check on main rotor disc plane angle of attack. If this angle is greater than zero then the experimental value for mean induced downwash is obtained from Table 1. Table 1 contains the tabular results of replotting the vortex-ring induced downwash data as a function of angle of attack and airspeed, instead of rate of descent and angle of attack. The experimental data is for angles of attack greater than or equal to 20 degrees and nondimensional airspeeds less than 3. Downwash values for an angle of attack of zero and for nondimensional airspeeds greater than 3 were added to the table based on momentum theory. If the angle of attack is less than zero, Table 1 is bypassed and momentum downwash is used.

The next step is to enter the low speed, low altitude tables. These are Tables 2, 3, 4 and 5. The value from Table 2, represents the change in steady induced downwash due to ground proximity. Curves were fitted to the data shown in Figure 6. These curves were then adjusted so that the values from the $h/d=1$ curve matched momentum theory values at the higher airspeeds tested. Then the values for each h/d curve were subtracted from momentum theory values to form incremental values. Even though the ground effect will exist at higher airspeeds, a conservative approach was taken by fairing all h/d curves into the momentum curve. Consequently at airspeeds above a nondimensional speed of 2.4, the incremental values go to zero for all h/d values. The increment in downwash from Table 2 is then added to the mean induced downwash from above to form a new mean induced downwash (inflow) term.

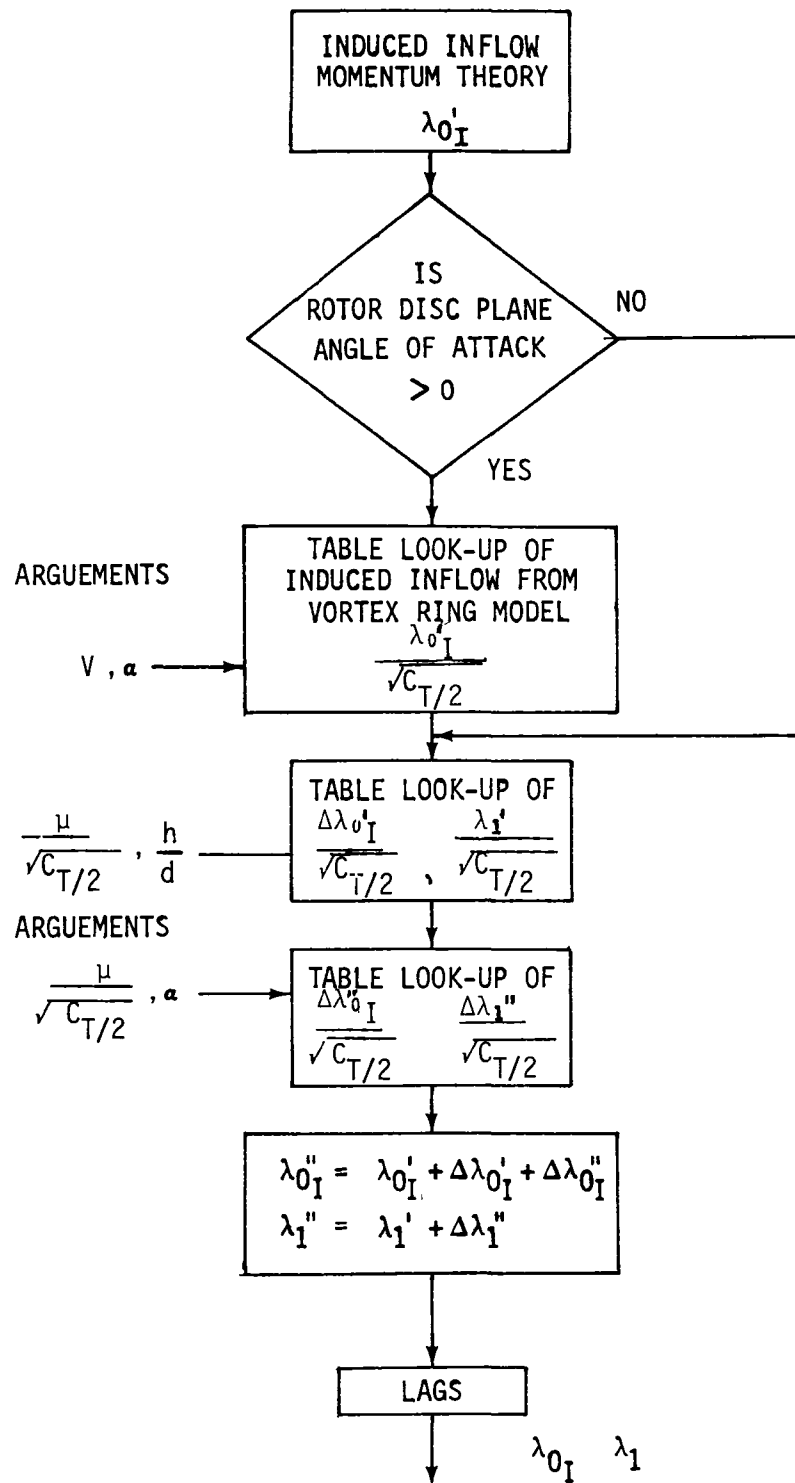


FIGURE 18. MODIFICATIONS TO SIMULATION MODEL.

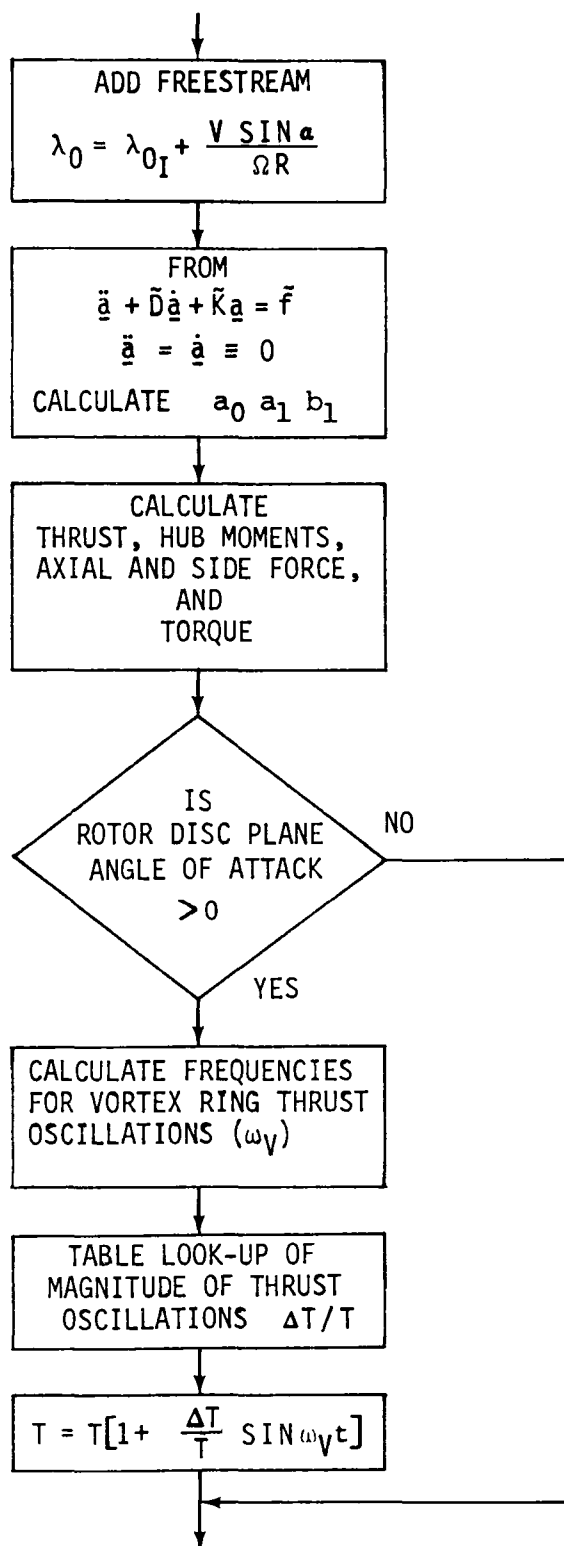


FIGURE 18. MODIFICATIONS TO SIMULATION MODEL (CONT)

		α								
		0	20	30	40	50	60	70	80	90
$V/\Omega R\sqrt{C_T/2}$.0	-1.000	-1.000	-1.000	-1.000	-1.000	-1.000	-1.000	-1.000	-1.000
	.1	-.998	-1.010	-1.005	-1.013	-1.008	-1.026	-1.056	-1.039	-1.090
	.2	-.990	-1.021	-1.010	-1.040	-1.042	-1.074	-1.104	-1.088	-1.170
	.3	-.978	-1.029	-1.040	-1.085	-1.103	-1.138	-1.167	-1.157	-1.220
	.4	-.961	-1.023	-1.070	-1.147	-1.188	-1.216	-1.256	-1.245	-1.290
	.5	-.940	-1.016	-1.125	-1.216	-1.288	-1.313	-1.350	-1.333	-1.360
	.6	-.914	-1.006	-1.180	-1.293	-1.393	-1.426	-1.457	-1.458	-1.460
	.7	-.886	-.982	-1.235	-1.380	-1.504	-1.539	-1.592	-1.595	-1.560
	.8	-.854	-.958	-1.290	-1.463	-1.609	-1.660	-1.732	-1.724	-1.670
	.9	-.821	-.931	-1.275	-1.521	-1.663	-1.773	-1.855	-1.844	-1.770
	1.0	-.786	-.894	-1.260	-1.519	-1.637	-1.787	-1.928	-1.953	-1.880
	1.1	-.751	-.857	-1.180	-1.479	-1.565	-1.712	-1.913	-2.062	-2.000
	1.2	-.716	-.819	-1.100	-1.376	-1.450	-1.575	-1.807	-2.145	-2.120
	1.3	-.681	-.782	-1.035	-1.262	-1.289	-1.413	-1.627	-2.096	-2.200
	1.4	-.648	-.737	-.970	-1.140	-1.150	-1.261	-1.445	-1.836	-2.300
	1.5	-.617	-.713	-.920	-1.037	-1.041	-1.131	-1.297	-1.562	-2.280
	1.6	-.587	-.675	-.870	-.946	-.944	-1.010	-1.165	-1.349	-2.130
	1.7	-.559	-.637	-.820	-.869	-.838	-.903	-1.043	-1.181	-1.750
	1.8	-.533	-.601	-.770	-.797	-.761	-.829	-.930	-1.031	-1.430
1.9	-.508	-.570	-.720	-.729	-.696	-.764	-.843	-.905	-1.160	
2.0	-.486	-.543	-.675	-.693	-.634	-.698	-.759	-.800	-.940	
2.4	-.411	-.450	-.553	-.552	-.506	-.519	-.528	-.549	-.565	
2.8	-.354	-.377	-.459	-.450	-.409	-.417	-.417	-.421	-.425	
3.2	-.311	-.321	-.390	-.371	-.345	-.349	-.348	-.350	-.351	
3.6	-.277	-.276	-.332	-.314	-.299	-.299	-.301	-.303	-.303	
4.0	-.250	-.251	-.287	-.271	-.263	-.265	-.267	-.268	-.268	
4.5	-.222	-.222	-.242	-.231	-.231	-.233	-.234	-.234	-.234	
5.0	-.200	-.200	-.208	-.205	-.206	-.207	-.208	-.209	-.209	
6.0	-.167	-.167	-.168	-.170	-.170	-.171	-.171	-.171	-.172	
9.0	-.111	-.112	-.112	-.112	-.112	-.112	-.112	-.112	-.113	

NOTES: (1) FOR $\alpha < 0$, USE MOMENTUM THEORY

(2) FOR $V/\Omega R/\sqrt{C_T/2} > 9.$, USE MOMENTUM THEORY

TABLE 1. STEADY INDUCED INFLOW RATIO IN
DESCENDING FLIGHT ($\lambda'_{0I}/\sqrt{C_T/2}$)

	h/d			
	0.4	0.6	0.7	1.0
$\mu/\sqrt{C_T/2}$ 0.00	0.2257	0.1275	0.0812	0.0009
0.10	0.2230	0.1272	0.0824	0.0039
0.20	0.2168	0.1274	0.0819	0.0025
0.30	0.2109	0.1248	0.0762	0.0022
0.40	0.2065	0.1223	0.0697	-0.0016
0.50	0.1942	0.1130	0.0604	-0.0076
0.60	0.1813	0.0992	0.0461	-0.0172
0.70	0.1640	0.0827	0.0295	-0.0349
0.80	0.1405	0.0602	0.0070	-0.0542
0.90	0.1163	0.0414	-0.0169	-0.0689
1.00	0.0926	0.0285	-0.0296	-0.0725
1.10	0.0768	0.0302	-0.0233	-0.0593
1.20	0.0688	0.0318	-0.0093	-0.0410
1.30	0.0631	0.0348	0.0040	-0.0232
1.40	0.0604	0.0355	0.0165	-0.0115
1.50	0.0605	0.0388	0.0207	-0.0067
1.60	0.0568	0.0385	0.0218	-0.0036
1.70	0.0527	0.0312	0.0214	-0.0009
1.80	0.0484	0.0290	0.0181	-0.0005
1.90	0.0397	0.0243	0.0131	-0.0023
2.00	0.0316	0.0129	0.0057	-0.0040
2.10	0.0236	0.0968	0.0043	-0.0030
2.20	0.0156	0.0645	0.0029	-0.0020
2.30	0.0078	0.0323	0.0014	-0.0010
2.40	0.0000	0.0000	0.0000	0.0000

- NOTES: (1) FOR $h/d > 1.0$, USE $\frac{h}{d} = 1$. VALUES
- (2) FOR $\mu/\sqrt{C_T/2} > 2.4$, $\Delta\lambda'_{0I}/\sqrt{C_T/2} = 0$
- (3) FOR $h/d < 0.4$, USE $h/d = 0.4$ VALUES
OR USE TRENDS TO EXTRAPOLATE TO
LOWER h/D VALUES

TABLE 2. CHANGE IN STEADY INDUCED INFLOW RATIO
DUE TO GROUND PROXIMITY ($\Delta\lambda'_{0I}/\sqrt{C_T/2}$)

	h/d			
	0.4	0.6	0.7	1.0
0.00	0.0000	0.0000	0.0000	0.0000
0.10	-0.0532	-0.2177	-0.1153	-0.1321
0.20	-0.1030	-0.3984	-0.2483	-0.2394
0.30	-0.1504	-0.5590	-0.4187	-0.3620
0.40	-0.2045	-0.7098	-0.6049	-0.4753
0.50	-0.2611	-0.8140	-0.7507	-0.5800
0.60	-0.3426	-0.9175	-0.8715	-0.6801
0.70	-0.4704	-1.0142	-0.9762	-0.7782
0.80	-0.7278	-1.1174	-1.0716	-0.8744
0.90	-0.9263	-1.2109	-1.1606	-0.9585
1.00	-1.0639	-1.2972	-1.2511	-1.0570
1.10	-1.1651	-1.3701	-1.3399	-1.1577
1.20	-1.2415	-1.4352	-1.3992	-1.2458
1.30	-1.2889	-1.4730	-1.4466	-1.3006
1.40	-1.3141	-1.4971	-1.4609	-1.3343
1.50	-1.3324	-1.4940	-1.4521	-1.3420
1.60	-1.3347	-1.4851	-1.4286	-1.3345
1.70	-1.3270	-1.4728	-1.4015	-1.3231
1.80	-1.3061	-1.4581	-1.3647	-1.3040
1.90	-1.2772	-1.4464	-1.3327	-1.2803
2.00	-1.2363	-1.4277	-1.2922	-1.2569
2.50	-1.0299	-1.2582	-1.0408	-1.0299
3.00	-0.7809	-0.9287	-0.7809	-0.7809
3.50	-0.6036	-0.6103	-0.6036	-0.6036
4.00	-0.4622	-0.4622	-0.4622	-0.4622
4.50	-0.3687	-0.3687	-0.3687	-0.3687
5.00	-0.3004	-0.3004	-0.3004	-0.3004
5.50	-0.2570	-0.2570	-0.2570	-0.2570
6.00	-0.2232	-0.2232	-0.2232	-0.2232

NOTES: (1) h/d > 1.0, USE h/d = 1.0 VALUES

$$(2) \mu/\sqrt{C_T/2} > 6. \quad \lambda'_1 = \sqrt{2}\lambda'_{0I} \left[\frac{\mu \cos \alpha}{(\lambda'_{0I} + \mu \sin \alpha)^2 + (\mu \cos \alpha)^2} \right]^{1/2}$$

TABLE 3. EFFECT OF GROUND PROXIMITY ON LONGITUDINAL FIRST HARMONIC INFLOW RATIO ($\lambda'_1/\sqrt{C_T/2}$)

	α		
	-10.6	1.0	6.0
$\mu/\sqrt{C_T/2}$ 0.00	-0.0138	0.0000	-0.0051
0.10	-0.0070	0.0000	-0.0033
0.20	-0.0018	0.0000	-0.0039
0.30	0.0081	0.0000	-0.0104
0.40	0.0422	0.0000	-0.0092
0.50	0.0795	0.0000	-0.0186
0.60	0.0947	0.0000	-0.0198
0.70	0.1023	0.0000	-0.0045
0.80	0.1086	0.0000	-0.0064
0.90	0.1041	0.0000	-0.0016
1.00	0.1029	0.0000	0.0025
1.10	0.0969	0.0000	0.0074
1.20	0.0984	0.0000	0.0202
1.30	0.1034	0.0000	0.0501
1.40	0.1277	0.0000	0.0849
1.50	0.1434	0.0000	0.1150
1.60	0.1380	0.0000	0.1108
1.70	0.1219	0.0000	0.1172
1.80	0.1050	0.0000	0.1050
1.90	0.0910	0.0000	0.0910
2.00	0.0710	0.0000	0.0710
2.20	0.0550	0.0000	0.0550
2.40	0.0471	0.0000	0.0471
2.60	0.0393	0.0000	0.0393
2.80	0.0314	0.0000	0.0314
3.00	0.0236	0.0000	0.0236
3.20	0.0157	0.0000	0.0157
3.40	0.0786	0.0000	0.0786
3.60	0.0393	0.0000	0.0393
3.80	0.0000	0.0000	0.0000
4.00	0.0000	0.0000	0.0000

- NOTES: (1) FOR $\mu/\sqrt{C_T/2} > 4$, $\Delta\lambda_{0I}''/\sqrt{C_T/2} = 0$
- (2) FOR $\alpha < -10.6$, ENTER TABLE 4 WITH $\alpha = -10.6$,
- (3) FOR $\alpha > 6$, ENTER TABLE 4 WITH $\alpha = 6$

TABLE 4. CHANGE IN STEADY INDUCED INFLOW RATIO
DUE TO ANGLE OF ATTACK ($\Delta\lambda_{0I}''/\sqrt{C_T/2}$)

	α		
	-10.6	1.0	6.0
$\mu/\sqrt{C_T/2}$ 0.00	0.0000	0.0000	0.0000
0.10	0.0000	0.0000	0.0000
0.20	0.0000	0.0000	0.0000
0.30	-0.0219	0.0000	-0.0219
0.40	-0.0597	0.0000	-0.0597
0.50	-0.1018	0.0000	-0.1018
0.60	-0.1375	0.0000	-0.1375
0.70	-0.1707	0.0000	-0.1707
0.80	0.0000	0.0000	0.0000
0.90	0.1094	0.0000	-0.0406
1.00	0.1811	0.0000	-0.0659
1.10	0.2325	0.0000	-0.1412
1.20	0.2726	0.0000	-0.1644
1.30	0.2886	0.0000	-0.1282
1.40	0.2885	0.0000	-0.1030
1.50	0.2958	0.0000	-0.0712
1.60	0.2892	0.0000	-0.0562
1.70	0.2861	0.0000	-0.0466
1.80	0.2690	0.0000	-0.0500
1.90	0.2507	0.0000	-0.0512
2.00	0.2234	0.0000	-0.0628
2.20	0.1377	0.0000	-0.0652
2.40	0.0870	0.0000	-0.0502
2.60	0.0524	0.0000	-0.0293
2.80	0.0308	0.0000	-0.0120
3.00	0.0162	0.0000	-0.0069
3.20	0.0062	0.0000	-0.0041
3.40	0.0008	0.0000	-0.0025
3.60	0.0000	0.0000	0.0000

- NOTES: (1) FOR $\mu/\sqrt{C_T/2} > 3.6$, $\Delta\lambda_1''/\sqrt{C_T/2} = 0$
- (2) FOR $\alpha < -10.6$, ENTER TABLE 5 WITH $\alpha = -10.6$
- (3) FOR $\alpha > 6$, ENTER TABLE 5 WITH $\alpha = 6$

TABLE 5. CHANGE IN LONGITUDINAL FIRST HARMONIC INFLOW RATIO DUE TO ANGLE OF ATTACK ($\Delta\lambda_1''/\sqrt{C_T/2}$)

Table 3 contains values for longitudinal inflow which were generated from curves faired through the data presented in Figure 7. As mentioned before in analyzing Figure 7, the values for $h/d = 1$ are considerably higher than the analytical values from Reference 3. There is no immediate explanation for this fact. Further investigation is recommended to determine whether this higher longitudinal inflow gradient does exist. The data for Table 3 was extended to higher airspeeds by fairing the curves into a curve generated from the theoretical expression of reference 3. Table 4 contains values representing changes in mean induced downwash due to angle of attack. Curves were faired through the data in Figure 9, and increments from the $\alpha=1$ curve were calculated and tabulated. Extending this data to higher angles of attack or lower angles of attack requires additional test data. Therefore, it is recommended at this time to use $\alpha = -10.6$ if $\alpha < -10.6$ and $\alpha = 6$ if $\alpha \geq 6$. This increment is added to the mean induced downwash, forming the final value for the steady induced inflow parameters.

Table 5 is the last of the low speed, low altitude tables. It contains incremental values of the longitudinal inflow coefficient due to angle of attack. Like Table 4, once the curves were fitted to the data of Figure 10, increments from the $\alpha=1$ curve were calculated and tabulated. The same comment about extending Table 4 applies to extending Table 5. The value from Table 5 is added to the value from Table 3 and λ_1'' , is obtained.

The steady induced inflow coefficient and the longitudinal inflow coefficient are next passed through first order lags, with approximately 0.3 second time constants, to account for air-mass dynamics. The lagged steady induced inflow is then added to the free-stream inflow and the total steady inflow coefficient is known. At this point the inflow model is completely defined.

The flapping equations are next used to calculate tip path plane orientation, assuming that \dot{a}_0 , \dot{a}_1 , and \dot{b}_1 are zero. Once this orientation in terms of the flapping coefficients a_0 , a_1 and b_1 is known, the main rotor forces and moments can be calculated. The thrust calculated at this point is the mean thrust value.

	α								
	0	20	30	40	50	60	70	80	90
.00	.000	.000	.000	.000	.000	.000	.000	.000	.000
.05	.000	.005	.003	.006	.008	.009	.009	.009	.012
.10	.000	.010	.006	.014	.017	.020	.024	.023	.026
.15	.000	.015	.011	.024	.029	.035	.041	.039	.044
.20	.000	.019	.016	.038	.043	.053	.060	.060	.062
.25	.000	.022	.024	.052	.060	.075	.082	.081	.084
.30	.000	.025	.032	.067	.081	.099	.105	.103	.103
.35	.000	.025	.048	.083	.103	.122	.129	.126	.125
.40	.000	.025	.064	.100	.126	.148	.153	.149	.145
.45	.000	.024	.078	.116	.152	.171	.182	.176	.170
.50	.000	.021	.092	.134	.175	.196	.213	.204	.194
.55	.000	.018	.100	.152	.201	.224	.243	.231	.215
.60	.000	.014	.108	.167	.226	.256	.271	.256	.230
.65	.000	.009	.113	.183	.249	.289	.295	.278	.242
.70	.000	.003	.117	.200	.270	.310	.315	.296	.250
.75	.000	.000	.119	.211	.288	.325	.329	.308	.258
.80	.000	.000	.120	.228	.303	.331	.337	.316	.262
.85	.000	.000	.116	.252	.316	.335	.342	.319	.264
.90	.000	.000	.112	.238	.322	.337	.344	.319	.260
.95	.000	.000	.103	.222	.323	.336	.341	.312	.250
1.00	.000	.000	.094	.214	.319	.333	.332	.303	.238
1.05	.000	.000	.077	.200	.308	.328	.323	.288	.225
1.10	.000	.000	.060	.183	.288	.318	.311	.272	.210
1.15	.000	.000	.030	.163	.260	.302	.295	.256	.195
1.20	.000	.000	.000	.132	.228	.284	.276	.237	.175
1.25	.000	.000	.000	.096	.193	.258	.248	.211	.150
1.30	.000	.000	.000	.060	.156	.222	.214	.182	.128
1.35	.000	.000	.000	.028	.116	.183	.181	.150	.103
1.40	.000	.000	.000	.000	.078	.144	.147	.115	.080
1.45	.000	.000	.000	.000	.039	.102	.113	.072	.055
1.50	.000	.000	.000	.000	.001	.061	.078	.041	.040
1.55	.000	.000	.000	.000	.000	.009	.040	.025	.030
1.60	.000	.000	.000	.000	.000	.000	.000	.013	.022
1.65	.000	.000	.000	.000	.000	.000	.000	.004	.016
1.70	.000	.000	.000	.000	.000	.000	.000	.000	.010
1.75	.000	.000	.000	.000	.000	.000	.000	.000	.007
1.80	.000	.000	.000	.000	.000	.000	.000	.000	.004
1.85	.000	.000	.000	.000	.000	.000	.000	.000	.002
1.90	.000	.000	.000	.000	.000	.000	.000	.000	.001
1.95	.000	.000	.000	.000	.000	.000	.000	.000	.000
2.00	.000	.000	.000	.000	.000	.000	.000	.000	.000

NOTES: (1) FOR $\alpha < 0$, $\Delta T/T = 0$

(2) FOR $V/\Omega R\sqrt{C_T/2} > 2$, $\Delta T/T = 0$

TABLE 6. MAGNITUDE OF THRUST FLUCTUATIONS IN DESCENDING FLIGHT ($\Delta T/T$)

Next the disc plane angle of attack is checked again. If this angle is positive, Table 6 which contains the magnitude of the thrust fluctuations is entered. Using the mean thrust value that has been calculated from the thrust equation and the calculated frequency for the thrust fluctuations, the instantaneous total thrust is found. During trim this portion of the modifications is bypassed. The modifications to account for the vortex-ring state and low speed, low altitude flight are at this point complete.

Simulation Results

Once the modifications were programmed and the coding verified, unpiloted maneuvers were performed. The UH-60 helicopter model was used for checkout purposes. First a low speed transition was tried with only the low speed, low altitude modifications engaged. Both in and out of ground effect transitions were performed. Figure 19 shows the required lateral stick to trim with air-speed for these two runs. Next a repeat run was made with the vortex-ring modifications also engaged to check the compatibility of the two effects. No complications arising from having both sets of modifications engaged were detected. A comparison of the improvement in matching flight test data is shown in Figure 20. Flight test points from reference 5 are compared to simulation results of before and after the modifications. If anything the low speed model tends to over predict the lateral stick migration slightly.

A piloted simulation followed, with Mr. Lynn Friesner, Boeing Vertol test pilot, assessing the model. Mr. Friesner is an experienced YUH-61A pilot with B0-105 time and has done extensive simulation work. When performing the low speed transition maneuver out of ground effect, he commented that he felt that the stick migration required to trim was consistent with his flight test experience. However, he felt that at low rotor heights, the sudden roll that he had expected was milder in the simulator. Several factors may have contributed to this perception. First, the aircraft used for simulation evaluation was the UH-60 which has a small hinge off-set articulated main rotor for which the roll response characteristics are less pronounced than on the hingeless configurations for which Mr. Friesner has experienced.

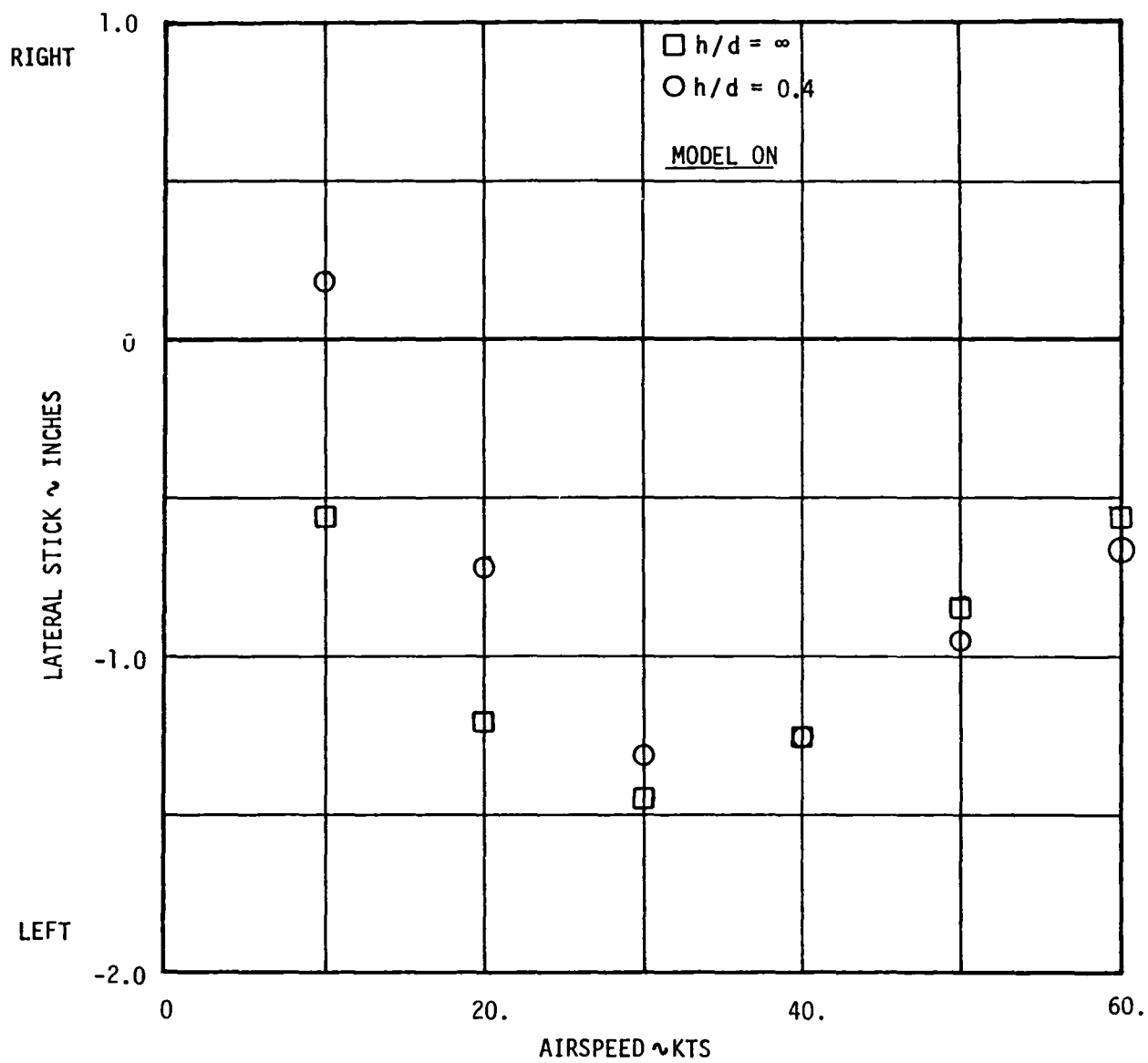


FIGURE 19. EFFECT OF GROUND PROXIMITY ON LATERAL TRIM.

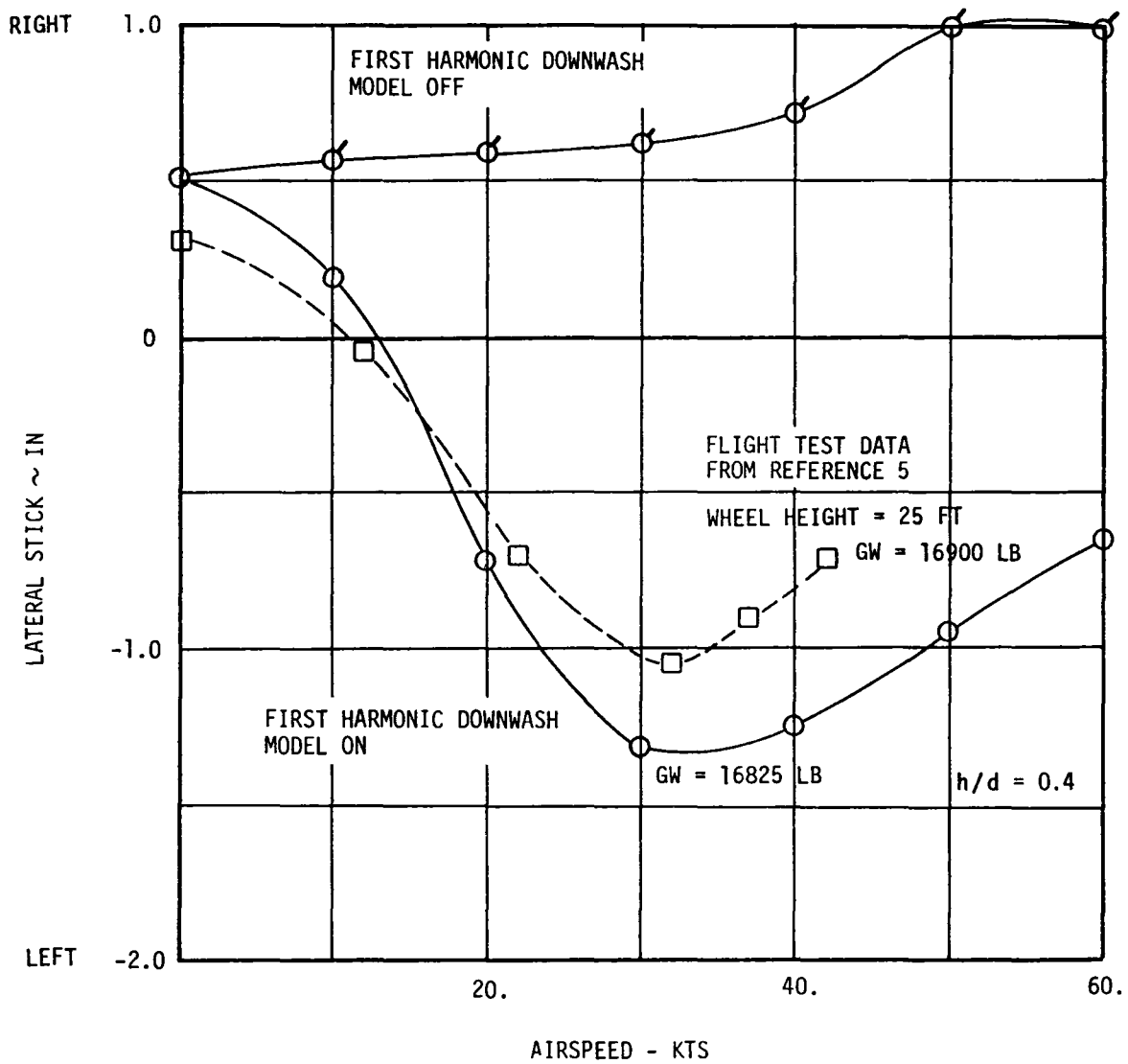


FIGURE 20. EFFECT OF MODIFICATIONS ON LATERAL TRIM

Secondly, Boeing Vertol's small motion simulator severely attenuates low frequency accelerations so that the perceived motion was reduced. Finally, the lowest value of rotor height to rotor diameter for which data existed was four tenths. Therefore, for any value less than four tenths, the tables are entered with a four tenths value as an argument and do not reflect potentially larger transients at h/d less than 0.4.

The vortex-ring modifications were also checked out unpiloted first. The simulator model was first trimmed at a constant rate of descent. Then the fly mode was engaged which resulted in the thrust fluctuations being calculated. Thrust and rate of descent during such a maneuver are shown for a high and low trimmed rate of descent in Figure 21. As can be seen, the thrust fluctuations are quite pronounced for the high rate of descent case. Figure 22 is another run whereby a step in collective was introduced to simulate an attempt at recovery from the high rate of descent. The rate of descent is seen to decrease almost immediately. And with this decrease in rate, the thrust fluctuations are reduced as expected. Next a set of trim runs, with and without the vortex-ring effect, were done at various rates of descent to assess the effect of the modification to mean induced downwash. Figure 23 shows the increase in power required when experimentally calculated induced downwash replaces that from momentum theory. This plot shows the so-called wasted power due to the vortex-ring state. These unpiloted runs indicated that the vortex-ring modifications were behaving as intended.

The piloted simulation to assess the vortex-ring state required that the pilot establish a rate of descent and then attempt to level off. Mr. Friesner had expected to find a rate of descent at which he had difficulty recovering. In fact, he expected to find a condition in which a pull-up in collective actually resulted in a higher rate of descent. This never occurred. No matter what the rate of descent, he had little trouble recovering. At one condition, he commented that he momentarily felt something like the vortex-ring problem, but all attempts to repeat the phenomenon failed. Subsequent examination of these runs showed that no engine power limit was included in the model. This would have enabled the pilot to pull unrealistically high power levels for recovery. The small vertical motion capability of the Boeing Vertol simulator

limits the simulator's ability to give vertical acceleration cues, and therefore may lead the pilot to perform unrealistic recovery profiles. Further simulation testing using a simulator with substantial "g" cues, and with a model having engine power limits is recommended.

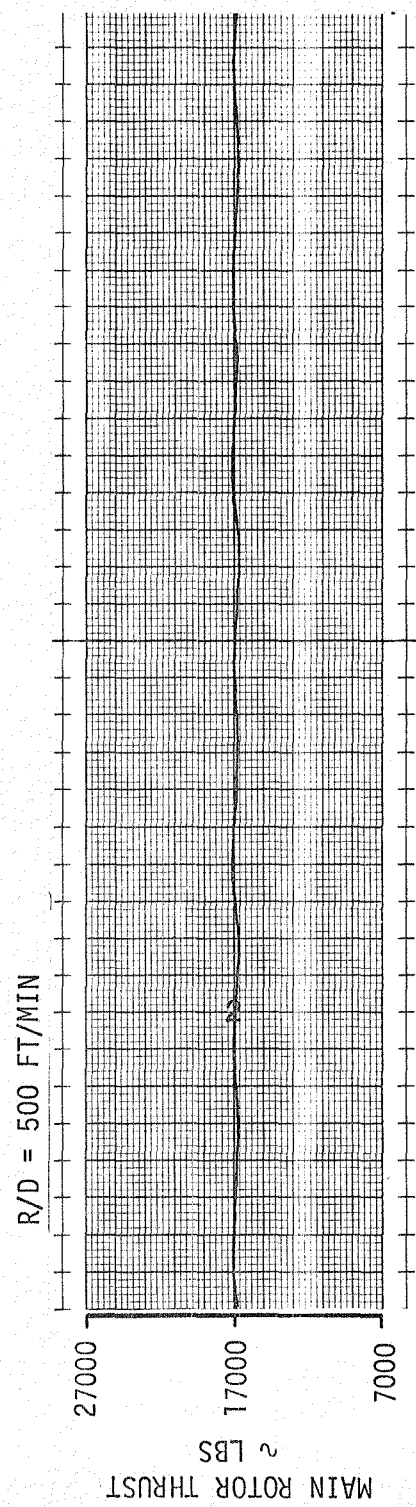
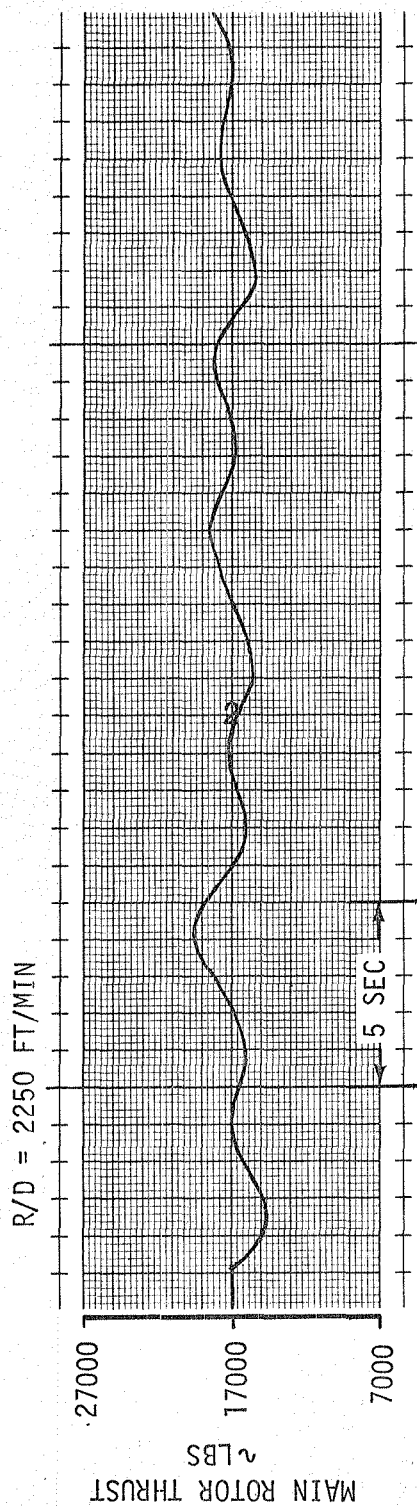


FIGURE 21. EFFECT OF RATE OF DESCENT ON THRUST FLUCTUATIONS

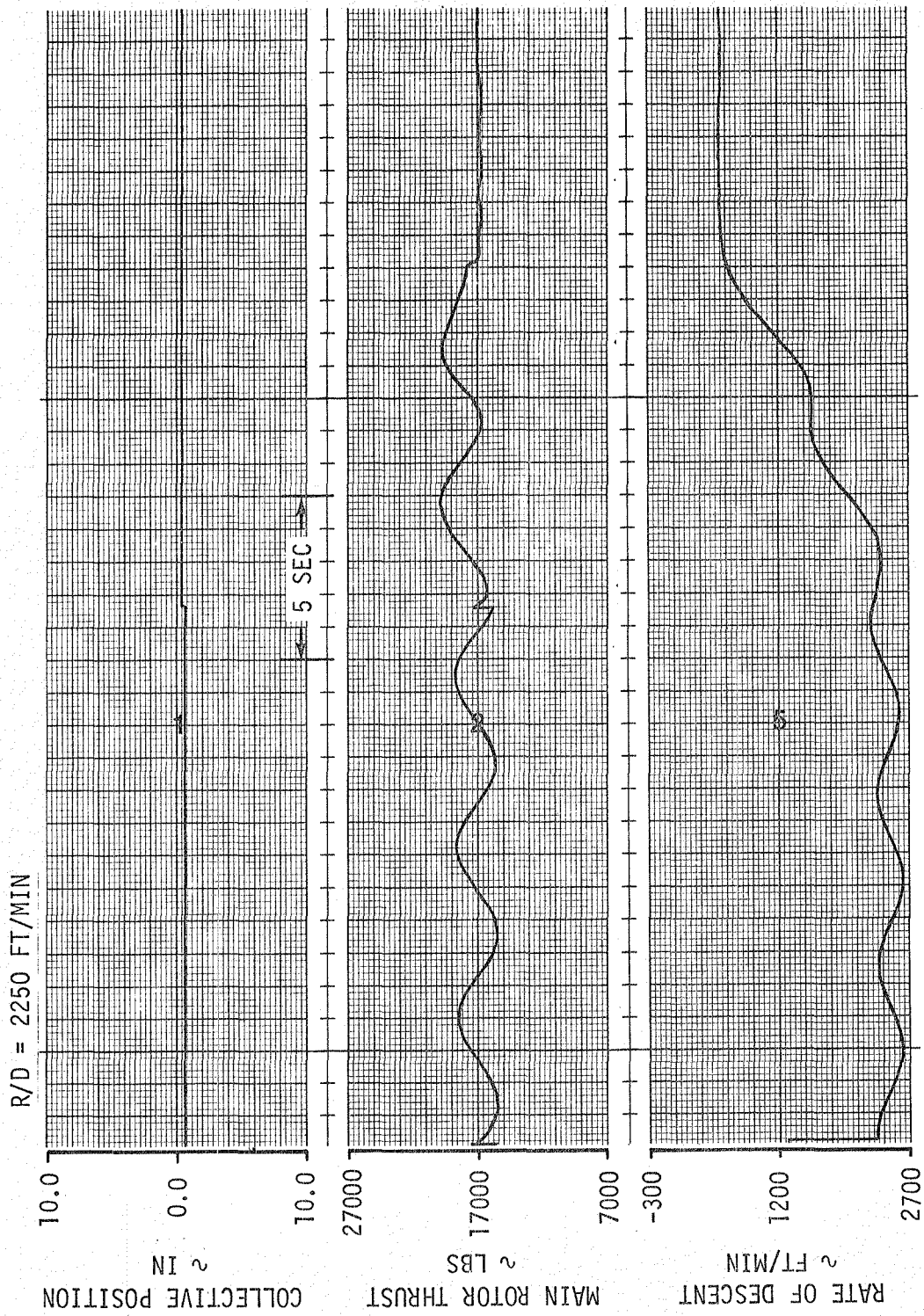


FIGURE 22. EFFECT OF A COLLECTIVE PULL UP AT A HIGH RATE OF DESCENT

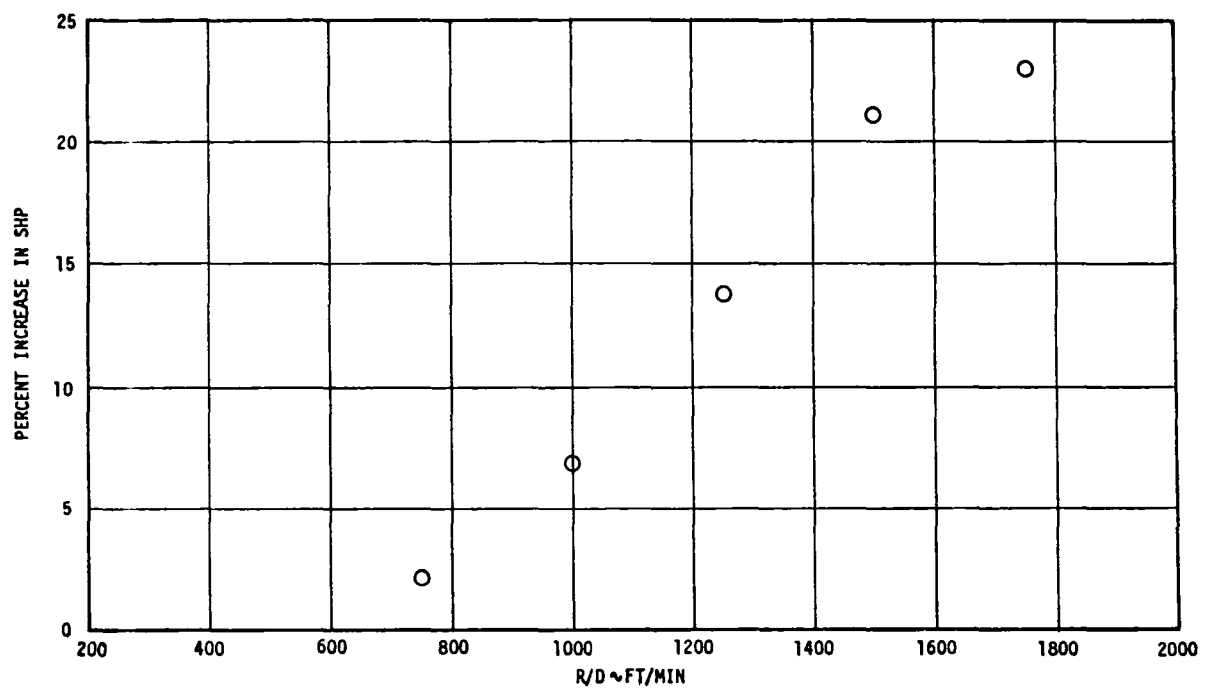


FIGURE 23. INCREASED POWER REQUIRED DUE TO VORTEX RING STATE

CONCLUSIONS

Based on the results of this effort, it is concluded that:

1. The low speed, low altitude modifications yield a lateral stick trim with airspeed requirement which is considered consistent with test results.
2. The in-ground effect portion of the low speed, low altitude tables may have to be extended if flight very close to the ground ($h/d < 0.4$) is desired. Extrapolation from data trends could be a first approximation.
3. The vortex-ring modifications produce the associated increases in power consistent with the test data of reference 4. However, difficulty during recovery from steep descending flight was not a problem on the Boeing Vertol simulator. Further investigation is recommended, varying aircraft configuration and flight condition.
4. The small vertical motion capability of the Vertol simulator with its washed out acceleration cues may have limited the pilot's feel of the thrust fluctuations associated with the vortex-ring state.
5. Further work is needed in the area of the frequency of the thrust fluctuations. More experimental data would be desirable. Perhaps a power spectral approach whereby a filter driven by white noise would yield better results. Another approach might be to investigate known or suspected problem areas by simulating with various frequency combinations and to observe their effect.
6. Both sets of modifications are capable of producing results consistent with the experimental data used to derive them.
7. Additional experimental data would be useful in expanding or verifying the tables presented here.

REFERENCES

1. Chen, R.T.N.; NASA TM 78575, 1979
A Simplified Rotor System Mathematical Model for Piloted Flight Dynamics Simulations
2. Sheridan, P.F.; USARTL TR 78-23, 1978
Interactional Aerodynamics of the Single Rotor Helicopter Configuration
3. Blake, B.B. and White, F.; American Helicopter Society, AHS 79-25, 1979
Improved Method of Predicting Helicopter Control Response and Gust Sensitivity
4. Washizu, J., Azuma, A., Koo, J., and Oka, T.; Journal of Aircraft, Vol. 3, No. 3, 1966
Experiments on a Model Helicopter Rotor Operating in the Vortex Ring State
5. Nagata, John I., etc.; USAAEFA Project No. 74-06-1, 1976
Government Competitive Test Utility
Tactical Transport Aircraft
System (UTTAS) Sikorsky YUH-60A
Helicopter
6. Chen, R.T.N., American Helicopter Society National Specialists Meeting, Rotor System Design, 1980
Selection of Some Rotor Parameters to Reduce Pitch-Roll Coupling of Helicopter Flight Dynamics

Item	Model Actual Values	Required Mach-Scaled Values
Radius	60 619 in.	60.619 in
Chord (reference)	4 742 in.	4 742 in.
Chord (overall tip)	4 790 in	4 790 in
Blade Number	4	4
Solidity	0 0996 ⁽¹⁾	0 0996
Effective Flap Hinge ⁽²⁾	0 162R	0.172R
Blade Weight ⁽³⁾	1 661 lb	1 665 lb
Weight Moment/Blade (flap)	3 208 ft-lb	3 201 ft-lb
Span CG (from C _L)	32 269 in	32 155 in
Span CG (from C _L)	0 532R	0 530R
Chordwise CG ⁽¹⁾	1 124 in.	1 110 in
Chordwise CG	0 2370C	0.2340C
Chordwise CG (dynamics)	0 2340C	0.2317C
Inertia/Blade (flap) ⁽³⁾	1,311 8 lb-in ²	1,290 7 lb-in ²
Inertia/Blade (pitch) ⁽⁴⁾	1 971 lb-in ²	-
<p>(1) Based on reference chord. (2) Based on analysis (L01) (3) Item is for blade portion outboard of 0 15 X/R and about 0 15 X/R (4) About quarter chord and for blade portion outboard of 0 15 X/R</p>		

TABLE A-1. MAIN ROTOR BLADE PHYSICAL PROPERTIES

RUN NO.	DISC LOADING (PSF)	ALPHA HUB (DEG)	H/D	ADVANCE RATIO	ROOT COLL.	A1C (DEG)	B1C (DEG)	MAIN ROTOR THRUST (LBS)	HUB ROLLING MOMENT (FT-LBS)	HUB PITCHING MOMENT (FT-LBS)
83	8.	-4.	0.4	0.011	15.3	-2.08	0.81	660.	-32.	-56.
				0.026	15.5	-1.93	0.88	723.	6.	-32.
				0.034	15.5	-2.02	0.88	730.	9.	-7.
				0.046	14.8	-1.94	0.86	695.	80.	33.
				0.056	14.6	-2.13	0.88	694.	107.	86.
				0.068	14.4	-1.95	0.92	665.	127.	112.
				0.078	14.1	-2.07	0.89	646.	123.	148.
				0.091	13.8	-1.97	0.86	675.	118.	154.
				0.112	13.5	-1.87	0.98	673.	115.	163.
84	8.	-4.	0.4	0.022	15.6	-1.94	0.87	700.	-6.	-33.
				0.028	15.6	-1.96	0.87	709.	-3.	-34.
				0.032	15.6	-1.98	0.86	712.	3.	-25.
				0.035	15.6	-2.16	0.85	713.	13.	2.
				0.040	15.3	-2.03	0.89	705.	44.	30.
				0.044	15.2	-1.97	0.91	710.	74.	50.
85	10.	-4.	0.4	0.015	17.0	-2.00	0.87	817.	-48.	-75.
				0.023	17.4	-2.04	0.89	892.	9.	-21.
				0.035	17.4	-2.04	0.91	898.	-13.	-4.
				0.043	16.9	-1.99	0.91	878.	42.	59.
				0.056	16.6	-1.99	0.90	868.	109.	102.
				0.068	16.3	-1.97	0.91	866.	147.	170.
				0.078	16.2	-1.92	0.93	856.	169.	204.
				0.088	16.0	-2.01	0.88	834.	151.	218.
				0.113	15.3	-1.89	0.94	827.	140.	236.
86	10.	-4.	0.4	0.044	16.8	-2.02	0.86	884.	40.	55.
				0.049	16.6	-2.05	0.82	898.	80.	89.
				0.054	16.5	-2.04	0.81	879.	94.	98.
				0.058	16.2	-2.02	0.84	849.	114.	109.
87	6.	-4.	0.4	0.016	14.0	-2.23	0.73	481.	-71.	-58.
				0.025	14.3	-2.04	0.81	578.	-22.	-34.
				0.034	14.0	-2.18	0.82	578.	5.	3.
				0.045	13.6	-1.96	0.94	541.	92.	42.
				0.056	13.2	-2.09	0.85	501.	85.	80.
				0.067	13.2	-1.91	0.93	501.	106.	113.
				0.077	12.9	-2.04	0.91	512.	97.	120.
				0.088	12.5	-2.03	0.90	522.	96.	119.
				0.111	12.2	-2.07	0.90	500.	67.	121.

TABLE A-2. WIND TUNNEL DATA USED IN THE DETERMINATION OF LOW SPEED, LOW ALTITUDE INFLOW COEFFICIENTS.

TABLE A-2.	RUN NO.	DISC LOADING (PSF)	ALPHA HUB (DEG)	H/D	ADVANCE RATIO	ROOT COLL.	A1C (DEG)	B1C (DEG)	MAIN ROTOR THRUST (LBS)	HUB ROLLING MOMENT (FT-LBS)	HUB PITCHING MOMENT (FT-LBS)	WIND TUNNEL DATA USED IN THE DETERMINATION OF LOW SPEED, LOW ALTITUDE INFLOW COEFFICIENTS (CONTINUED)
	88	6.	-4.	0.4	0.039	13.6	-1.89	0.90	553.	49.	32.	
0.037					13.8	-2.01	0.86	578.	31.	10.		
0.030					14.0	-1.90	0.90	567.	7.	-20.		
0.026					14.0	-1.87	0.92	557.	-0.	-34.		
	89	4.	-4.	0.4	0.024	12.2	-1.89	0.89	383.	-3.	-38.	
0.033					11.9	-1.91	0.93	388.	68.	14.		
0.045					11.9	-2.05	0.84	373.	76.	49.		
0.056					11.6	-2.07	0.84	348.	78.	70.		
0.066					11.3	-1.91	0.90	366.	81.	94.		
0.077					11.1	-1.91	0.92	363.	81.	91.		
0.089					10.9	-1.96	0.88	343.	66.	91.		
0.111					10.9	-1.99	0.89	350.	52.	79.		
0.027					12.1	-2.07	0.83	392.	-1.	-11.		
	92	8.	-10.6	0.4	0.010	17.4	-1.88	0.80	630.	-69.	-114.	
0.024					17.0	-1.67	0.86	696.	-19.	-76.		
0.033					16.9	-1.85	0.80	726.	-5.	-33.		
0.045					16.7	-1.89	0.78	713.	59.	12.		
0.056					16.5	-1.68	0.91	694.	91.	45.		
0.068					16.5	-1.70	0.83	667.	75.	79.		
0.078					16.4	-1.66	0.89	687.	96.	113.		
0.090					16.1	-1.79	0.78	655.	73.	118.		
0.109					15.9	-1.71	0.81	661.	63.	123.		
	93	8.	6.	0.4	0.015	16.6	-1.90	0.84	626.	-61.	-118.	
0.021					16.6	-1.91	0.84	696.	-31.	-69.		
0.034					16.4	-2.08	0.89	699.	-24.	-43.		
0.046					15.8	-1.74	0.86	691.	86.	27.		
0.056					15.8	-1.83	0.77	697.	109.	61.		
0.066					15.2	-1.88	0.86	692.	160.	149.		
0.078					14.6	-1.88	0.80	675.	150.	162.		
0.088					13.9	-1.71	0.86	650.	146.	159.		
0.109					13.1	-1.72	0.86	661.	145.	136.		

TABLE A-2.	RUN NO.	DISC LOADING (PSF)	ALPHA HUB (DEG)	H/D	WIND TUNNEL DATA USED IN THE DETERMINATION OF LOW SPEED, LOW ALTITUDE INFLOW COEFFICIENTS (CONTINUED)						
					ADVANCE RATIO	ROOT COLL.	AIC (DEG)	BIC (DEG)	MAIN ROTOR THRUST (LBS)	HUB ROLLING MOMENT (FT-LBS)	HUB PITCHING MOMENT (FT-LBS)
94	8.	1.	0.4		0.014	16.6	-1.74	0.83	632.	-59.	-106.
					0.023	16.7	-1.85	0.86	687.	-35.	-80.
					0.035	16.6	-1.80	0.85	699.	-9.	-34.
					0.045	16.1	-1.78	0.82	692.	52.	2.
					0.056	15.9	-1.98	0.78	665.	104.	50.
					0.068	15.5	-1.89	0.82	669.	131.	115.
					0.078	15.2	-1.83	0.83	627.	127.	125.
					0.088	14.8	-1.92	0.78	624.	118.	130.
					0.111	14.0	-1.77	0.85	644.	110.	131.
95	8.	1.	0.4		0.027	16.7	-1.67	0.91	699.	-25.	-76.
					0.032	16.6	-1.73	0.88	713.	-27.	-56.
					0.036	16.6	-1.84	0.89	712.	-21.	-50.
					0.039	16.2	-1.59	0.83	682.	9.	-27.
					0.026	16.7	-1.65	0.86	686.	-12.	-55.
					0.030	16.7	-1.80	0.86	680.	-17.	-46.
96	8.	1.	0.4		0.036	16.8	-1.66	0.90	706.	-8.	-40.
					0.041	16.6	-1.78	0.69	721.	-2.	-12.
					0.050	16.1	-1.50	0.84	703.	91.	35.
					0.053	15.8	-1.63	0.85	654.	93.	76.
					0.058	15.7	-1.68	0.88	668.	99.	87.
					0.062	15.7	-1.86	0.79	690.	100.	109.
97	8.	1.	0.4		0.023	16.9	-2.01	0.83	695.	-32.	-37.
					0.027	16.9	-1.98	0.85	715.	-26.	-31.
					0.031	16.6	-1.92	0.85	689.	-20.	-24.
					0.037	16.6	-1.97	0.82	694.	-23.	-10.
					0.044	16.6	-1.96	0.81	730.	32.	21.
					0.045	16.3	-1.88	0.87	712.	66.	35.
					0.048	16.3	-1.86	0.87	717.	78.	44.
					0.054	16.0	-1.70	0.97	683.	118.	64.
					0.058	15.8	-1.91	0.85	674.	109.	79.
					0.063	15.8	-1.99	0.81	696.	120.	103.

TABLE A-2. WIND TUNNEL DATA USED IN THE DETERMINATION OF LOW SPEED, LOW ALTITUDE INFLOW COEFFICIENTS (CONTINUED)											
RUN NO.	DISC LOADING (PSF)	ALPHA HUB (DEG)	H/D	ADVANCE RATIO	ROOT COLL.	A1C (DEG)	B1C (DEG)	MAIN ROTOR THRUST (LBS)	HUB ROLLING MOMENT (FT-LBS)	HUB PITCHING MOMENT (FT-LBS)	
101	8.	1.	0.4	0.008	16.5	-1.78	0.83	632.	-60.	-102.	
				0.023	16.5	-1.68	0.84	678.	-25.	-52.	
				0.035	16.5	-1.77	0.80	693.	-14.	-19.	
				0.045	16.0	-1.83	0.82	695.	68.	28.	
				0.055	15.8	-2.01	0.73	693.	96.	62.	
				0.067	15.4	-1.96	0.76	663.	128.	116.	
				0.089	14.5	-1.90	0.80	597.	119.	133.	
				0.113	13.7	-1.74	0.84	628.	106.	131.	
102	8.	1.	0.6	0.008	17.1	-1.78	0.84	682.	-52.	-23.	
				0.022	17.0	-1.89	0.85	768.	8.	49.	
				0.035	16.7	-1.89	0.79	750.	54.	93.	
				0.045	16.3	-1.80	0.83	726.	91.	126.	
				0.055	16.3	-1.56	0.83	699.	116.	164.	
				0.068	15.7	-1.66	0.83	695.	145.	213.	
				0.077	15.3	-1.78	0.79	672.	134.	225.	
				0.088	14.8	-1.88	0.76	702.	134.	235.	
0.112	13.8	-1.81	0.79	677.	113.	220.					
103	8.	1.	0.7	0.011	17.1	-1.88	0.74	643.	-64.	-86.	
				0.022	17.1	-1.93	0.69	718.	15.	4.	
				0.031	16.9	-2.13	0.69	724.	50.	24.	
				0.044	16.5	-1.97	0.72	683.	84.	88.	
				0.056	16.3	-1.85	0.79	655.	111.	113.	
				0.067	16.1	-1.85	0.80	723.	161.	160.	
				0.078	15.4	-1.97	0.76	668.	149.	170.	
				0.089	14.9	-1.88	0.81	693.	151.	181.	
0.112	14.0	-2.02	0.65	662.	99.	146.					
105	8.	1.	1.0	0.109	14.5	-1.71	0.83	672.	112.	170.	
				0.087	15.6	-1.65	0.82	708.	149.	181.	
				0.076	16.0	-1.57	0.86	719.	159.	166.	
				0.069	16.3	-1.85	0.74	711.	126.	147.	
				0.054	16.5	-1.76	0.80	666.	92.	92.	
				0.045	16.8	-1.74	0.82	671.	68.	55.	
				0.034	17.0	-1.69	0.85	678.	47.	12.	
				0.023	17.0	-1.79	0.78	692.	1.	-14.	
				0.009	17.2	-1.68	0.85	697.	-46.	-77.	

1 Report No NASA CR-166385	2 Government Accession No	3 Recipient's Catalog No	
4 Title and Subtitle Math Modeling for Helicopter Simulation of Low Speed, Low Altitude and Steeply Descending Flight		5 Report Date July 1982	6 Performing Organization Code
		8 Performing Organization Report No	10 Work Unit No
7 Author(s) Philip R. Sheridan, Carl Robinson, Dr. John Shaw, Fred White		11 Contract or Grant No NAS2-10975	
		13 Type of Report and Period Covered Contractor Report - Final Report	
9 Performing Organization Name and Address Boeing Vertol Company P. O. Box 16858 Philadelphia, Pennsylvania		14 Sponsoring Agency Code	
		12 Sponsoring Agency Name and Address National Aeronautics and Space Administration Washington, D. C. 20546	
15 Supplementary Notes Technical Monitor: William A. Decker, Mail Stop 211-2 FTS 448-5362 NASA Ames Research Center, Moffett Field, CA 94035 (415)965-5362			
16 Abstract A math model has been formulated to represent some of the aerodynamic effects of low speed, low altitude, and steeply descending flight. The formulation is intended to be consistent with the single rotor real time simulation model at NASA Ames Research Center. The effect of low speed, low altitude flight on main rotor downwash was obtained by assuming a uniform plus first harmonic inflow model and then by using wind tunnel data in the form of hub loads to solve for the inflow coefficients. The result was a set of tables for steady and first harmonic inflow coefficients as functions of ground proximity, angle of attack, and airspeed. The aerodynamics associated with steep descending flight in the vortex-ring state were modeled by replacing the steady induced downwash derived from momentum theory with an experimentally derived value and by including a thrust fluctuations effect due to vortex shedding. Tables of the induced downwash and the magnitude of the thrust fluctuations were created as functions of angle of attack and airspeed.			
17 Key Words (Suggested by Author(s)) Helicopter Handling Qualities Math Model Helicopter Dynamics Flight Simulation		18 Distribution Statement Unlimited Distribution Subject Category 08	
19 Security Classif (of this report) Unclassified	20 Security Classif (of this page) Unclassified	21 No of Pages	22 Price*

End of Document